JGR Solid Earth

RESEARCH ARTICLE
10.1029/2018JB016543

Key Points:
- Breakdown of earthquake self-similar scaling was observed in the 2016–2017 central Italy seismic sequence
- Source rupture directivity in 14 events was identified according to the azimuthal variation of apparent source spectra
- Ten events were characterized by unilateral rupture mostly in the NNW direction and fast rupture velocity

Supporting Information:
- Supporting Information S1

Correspondence to:
Y. Ren,
renyefei@iem.ac.cn

Citation:
Wang, H., Ren, Y., Wen, R., & Xu, P. (2019). Breakdown of earthquake self-similar scaling and source rupture directivity in the 2016–2017 central Italy seismic sequence. *Journal of Geophysical Research: Solid Earth*, *124*. https://doi.org/10.1029/2018JB016543

Received 13 AUG 2018
Accepted 26 MAR 2019
Accepted article online 29 MAR 2019

Breakdown of Earthquake Self-Similar Scaling and Source Rupture Directivity in the 2016–2017 Central Italy Seismic Sequence

Hongwei Wang[1,2], **Yefei Ren**[1,2], **Ruizhi Wen**[1,2], **and Peibin Xu**[1,2]

[1]Institute of Engineering Mechanics, China Earthquake Administration, Harbin, China, [2]Key Laboratory of Earthquake Engineering and Engineering Vibration of China Earthquake Administration, Harbin, China

Abstract To analyze the source characteristics of the 2016–2017 central Italy seismic sequence, source spectra of 78 earthquakes of $M_L = 3.5–6.1$ were separated from the S wave Fourier spectra using the two-step nonparametric generalized inversion technique. Source parameters (e.g., stress drop) were estimated from the source spectra following the ω-square model. Stress drops were found mainly in the range 0.113–12.190 MPa. The significant dependence of stress drop on magnitude indicates the breakdown of earthquake self-similar scaling in this sequence. The low stress drops for small events following the release of high stress by the mainshock might have led to stress accumulation on the unruptured fault, which could explain the subsequent occurrence of multiple major events. We investigated the source rupture directivity for 36 events through the azimuthal variation of apparent source spectra. Significant variation was observed at specific frequency bands (generally, over corner frequencies) in 10 events caused by rupture directivity, which was verified by the stable estimation of rupture plane. The rupture parameters confirmed unilateral ruptures predominantly on the NNW–SSE striking fault with fast rupture velocity (2.52–2.84 km/s) for the 10 events. Rupture parameters for an additional four events with stable estimated rupture plane were also analyzed. These were characterized by slow rupture velocity causing weak directivity effects. According to the rupture parameters for the 14 events, prevailing SSE or SEE (NNW or NNE) rupture directivity was a common feature for events to the north (south) of the mainshock in this earthquake sequence.

1. Introduction

The 2016–2017 central Italy seismic sequence was initiated by an M_L 6.0 mainshock on 24 August 2016 at 01:36:32 (UTC) close to the town of Accumoli. About 2 months later, another two destructive earthquakes (M_L 5.9 on 26 October at 19:18:06 [UTC] near the town of Visso and M_L 6.1 on 30 October at 06:40:18 [UTC] near the town of Norcia) subsequently shocked the area to the NNW of the M_L 6.0 event. The largest magnitude event (M_L 6.1) in this sequence occurred between the epicenters of the M_L 6.0 and M_L 5.9 events. On 18 January 2017, a further four moderate events of $M_L > 5.0$ struck the southernmost portion of this sequence. Up until 24 August 2017, this sequence comprised ~1,100 events of $M_L \geq 3.0$ (http://cnt.rm.ingv.it), primarily nucleated at a depth of about 7–12 km. This sequence progressively activated ~80-km-long NNW–SSE trending normal fault systems that included the Mt. Vettore-Mt. Bove fault system and the Laga Mts. fault system, which generally strike ~N155° and dipping ~50° toward the southwest (Cheloni et al., 2017; Chiaraluce et al., 2017; Pizzi et al., 2017; Tinti et al., 2016). Strong interaction between the preexisting compressional thrusts and the younger and active normal faults explains the seismicity pattern of this sequence (Chiaraluce et al., 2017; Pizzi et al., 2017). According to the time domain moment tensor solutions reported by the Istituto Nazionale di Geofisica e Vulcanologia (INGV), most ruptures in this sequence share similar normal-faulting mechanisms, whereas a few represent strike-slip events.

Central Italy, one of the most seismically active regions in Italy, has previously suffered a series of moderate historical and instrumental events, including the 2009 M_w 6.1 L'Aquila earthquake (Chiarabba et al., 2009) and the 1997 M_w 6.0 Colfiorito earthquake as part of the Umbria-Marche sequence (Amato et al., 1998). The 2016–2017 central Italy seismic sequence filled exactly the spatial seismic gap between the ruptures of the southern 2009 L'Aquila sequence and the northern 1997 Umbria-Marche sequence (shown in Figure 1). The M_w 6.2 Amatrice event, which occurred in 1639, was the event closest to the epicenter of the M_L 6.0 mainshock of the 2016–2017 sequence (Rovida et al., 2016). The seismogenic area of the 2016–2017 sequence is characterized as having high seismic hazard. The horizontal peak ground acceleration (PGA) with 10%

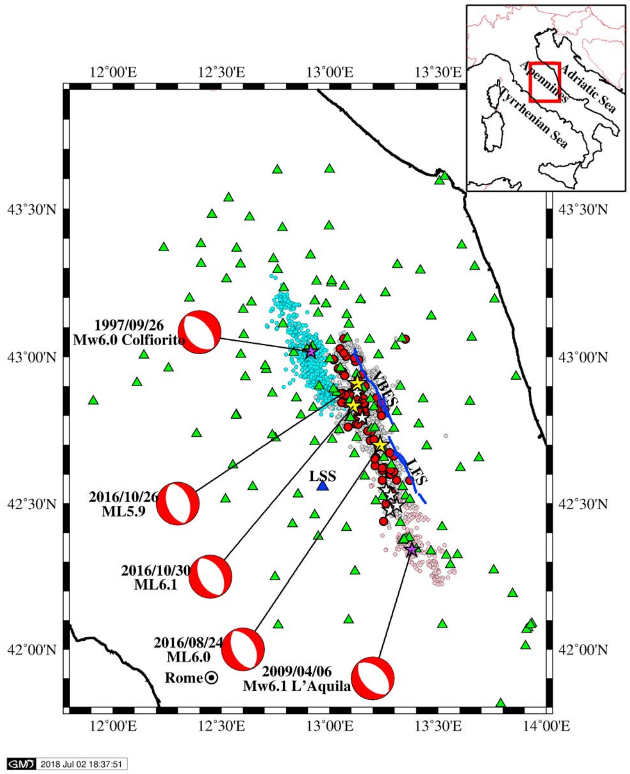

Figure 1. Locations of epicenters of earthquakes (red dots and yellow and white stars) and strong-motion stations (triangles) considered in the spectral inversion analysis of our study. Gray, cyan, and pink dots represent events in the 2016–2017 central Italy, 1997 Umbria-Marche and 2009 L'Aquila seismic sequences, respectively. Yellow stars represent three major earthquakes (M_L = 6.0, 5.9, and 6.1), and white stars represent six events of $M_L > 5.0$. Purple stars represent the 2009 M_w 6.1 L'Aquila and 1997 M_w 6.0 Colfiorito earthquakes. VBFS and LFS represent the Mt. Vettore-Mt. Bove fault system and the Laga Mts. fault system, respectively. Focal mechanisms shown were derived from the time domain moment tensor catalog of the Istituto Nazionale di Geofisica e Vulcanologia, except that of the Colfiorito earthquake, which was derived from the Global Centroid-Moment-Tensor catalog. Station LSS marks the reference site used in this study. In the insert map, the red rectangle indicates the location of the study region within Italy.

probability of exceedance in 50 years on hard ground with $V_{S30} > 800$ m/s (where V_{S30} is the time-weighted average shear-wave velocity over the uppermost 30 m at the site) has been evaluated as 0.250–0.275 g (where g is gravitational acceleration), that is, the submaximal level on the seismic hazard map of Italy (Stucchi et al., 2011).

The study of source characteristics represents an important basis for interpretation of seismic damage and earthquake physics. For example, Luzi et al. (2017) ascribed the anisotropic distribution of observed ground motions in three major events in the 2016–2017 central Italy seismic sequence to near-source effects (i.e., directivity, hanging-wall, and fling-step effects). Immediately after the M_L 6.0 mainshock and ongoing aftershocks, studies were performed to investigate the source characteristics of this sequence. The kinematic source models for the M_L 6.0 mainshock and two subsequent major earthquakes (M_L 5.9 and 6.1) were inverted using near-source strong-motion data, teleseismic waveforms, and geodetic data to reveal the slip heterogeneity, rupture directivity, and seismogenic mechanism (Chiaraluce et al., 2017; Liu et al., 2017; Pizzi et al., 2017; Scognamiglio et al., 2018; Tinti et al., 2016). According to analyses of the spatial distributions of various ground-motion intensity measures, Ren et al. (2017) both confirmed the asymmetrical bilateral rupture propagation of the M_L 6.0 mainshock and explained the directivity effects, especially on short-period ground motions. Similarly, Convertito et al. (2017) inferred the horizontal source rupture directivity of the M_L 6.0 mainshock by analyzing the peak ground velocity, and they suggested a contribution from the dynamic strain, enhanced by rupture directivity, to the occurrence of the ongoing aftershocks. Calderoni et al. (2017) estimated the rupture directivity of 16 of the strongest events in this sequence by investigating the S wave amplitude variations versus azimuths, and they confirmed persistent along-strike rupture directivity of normal-faulting earthquakes in the Apennines.

The source characteristics (i.e., earthquake self-similar scaling and source rupture directivity) of the 1997 Umbria-Marche and 2009 L'Aquila seismic sequences in central Italy have been investigated in many studies that have considered the estimation of earthquake hazard (e.g., Bindi et al., 2001, 2004, 2009; Calderoni et al., 2015; Cultrera et al., 2009; Pacor, Spallarossa, et al., 2016, Pacor, Gallovič, et al., 2016). In this study, we attempted to investigate the source characteristics of the 2016–2017 central Italy seismic sequence based on source spectra separated from the S wave Fourier amplitude spectra using a nonparametric generalized inversion technique (GIT). The earthquake self-similar scaling in this sequence was evaluated from the dependence of the stress drop on moment magnitude, and the source rupture directivity was discussed according to the variations of the apparent source spectra versus the station azimuths.

2. Data Set

Large numbers of strong-motion data from the 2016–2017 central Italy seismic sequence were recorded by the National Accelerometric Network operated by the Italian Department of Civil Protection, National Seismic Network and Mediterranean Very Broadband Seismographic Network operated by the INGV, North-East Italy Seismic Network operated by the Istituto Nazionale di Oceanografia e di Geofisica Sperimentale, and an additional 17 temporary stations installed immediately after the mainshock in the epicentral area by the INGV. With respect to this sequence, the Engineering Strong-Motion database (http://esm.mi.ingv.it) was formally released. It comprised about 8,000 high-quality, manually processed strong-motion recordings with hypocentral distances (R) within the range 6.2–429.5 km, collected at 337 stations in 106 shallow crustal events of M_L = 3.1–6.1. The data processes performed in producing the Engineering

Strong-Motion database mainly consisted of baseline correction and Butterworth band-pass filtering. Generally, the low-cut corner frequencies (f_L) were found <0.2 Hz and the high-cut corner frequencies were found equal to 30 Hz for most recordings.

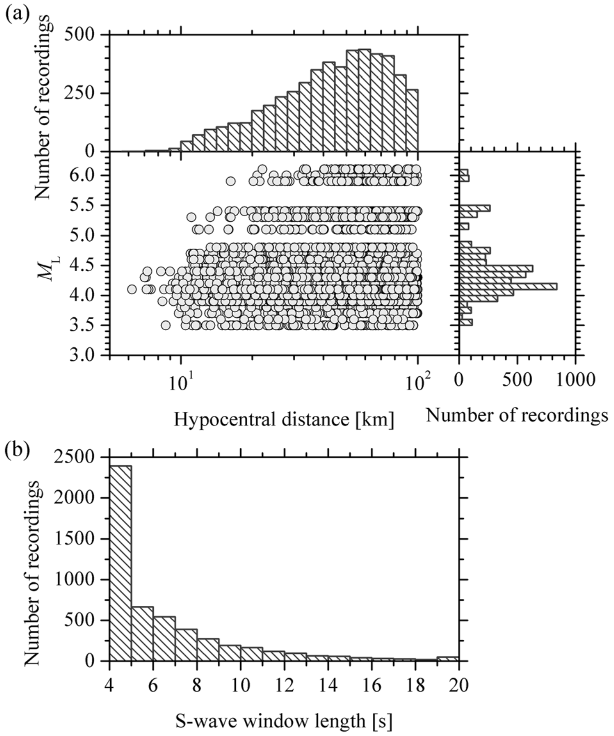

Figure 2. (a) Hypocenter distance versus local magnitude (M_L) for the recordings considered in this study. Histograms of the hypocenter distance and local magnitude for the selected recordings are also plotted.
(b) Histogram of *S* wave window lengths of the recordings used in this study.

For the purposes of spectral inversion analysis, we selected 5,135 ground-motion recordings obtained at 142 surface stations during 78 events of $M_L = 3.5–6.1$ (as shown in Figure 1) based on the following criteria: (1) maximal horizontal PGA < 100 cm/s^2; (2) hypocentral distance $R \leq 100$ km; and (3) given criteria (1) and (2), each selected event had to be recorded by at least 10 of the considered stations, each of which recorded at least 10 of the selected events. We selected recordings with PGA < 100 cm/s^2 to avoid the existence of nonlinear soil behavior as much as possible. As is well known, site response, not only in terms of amplitude but also in relation to fundamental frequency, can show significant variation because of soil nonlinearity caused by strong ground shaking (Beresnev et al., 1995; Régnier et al., 2013; Ren et al., 2017). Thus, the variation of site response due to nonlinear soil behavior in some strong recordings could bias the trade-off between the inverted site response and source spectra. As proposed by McNamara et al. (2012), crustal *S* waves are the predominant phase on seismograms at distances of <100 km. The *Lg* develops while crustal *S* waves are still present at distances of 100–250 km, whereas crustal *Lg* is dominant on seismograms beyond 250 km. Here recordings of $R \leq 100$ km were considered to reduce contamination from *Lg* to the applied *S* wave as much as possible. Figure 2a shows M_L-R plots of the selected recordings. Most recordings were obtained from earthquakes of $M_L = 4.0–4.5$. The hypocentral distances mainly covered the range 20–100 km, and near-source recordings ($R < 10$ km) were very limited. The minimum distance of the selected recordings was 6.2 km.

We extracted the *S* waves of the horizontal components of the selected recordings, and we computed the *S* wave Fourier amplitude spectra at 300 frequencies uniformly spaced on the logarithmic scale from 0.25–30 Hz. The *S* wave arrival time was identified as the point of abrupt increase in the Husid plots, which show the cumulative integral of squared acceleration (Husid, 1967). The *S* wave end time was determined as the point when the particular proportion of the total wave energy was reached. In this study, we adopted the distance-dependent proportions proposed by Pacor, Spallarossa, et al. (2016) to distinguish the *S* wave end time of the L'Aquila recordings, that is, 90% for $R < 25$ km, 80% for $R = 25–50$ km, and 70% for $R > 50$ km. We stipulated the *S* wave window length had to be at least 4 s to guarantee spectral resolution up to 0.25 Hz, and the maximal *S* wave window length was fixed to 20 s to minimize coda-wave effects. The histogram of the *S* wave window lengths for the selected recordings is shown in Figure 2b. The *S* wave window lengths of about half the selected recordings are 4–5 s. The short-period *S* waves could be ascribed to the fact that the bulk of recordings was obtained from small events of $M_L < 5.0$. A cosine taper was added at both the beginning and end of the extracted *S* waves to eliminate truncation errors, and the length of each taper was 10% of the *S* wave window length. The calculated Fourier amplitude spectra of the *S* waves were smoothed using the windowing function of Konno and Ohmachi (1998) with $b = 20$. The root mean square average of the Fourier amplitude spectra at two horizontal components was used to represent the horizontal ground motion in the frequency domain. Figure 3 provides two examples of *S* wave extractions and the calculated horizontal Fourier spectra. The identified *S* wave windows are highlighted in this figure.

Pre–*P* wave noise windows of the same length as the *S* wave windows were used to calculate the signal-to-noise ratios (SNRs). Criteria of an SNR threshold of 5.0 and usable frequency no smaller than $1.25f_L$ (Abrahamson & Silva, 1997) were adopted simultaneously to select the usable portion of the Fourier spectra. Figure 3 illustrates the usable portion of the Fourier spectra of the two example *S* waves according to the thresholds of SNRs and f_L. It can be seen that the entire frequency band of 0.25–30 Hz is usable for the

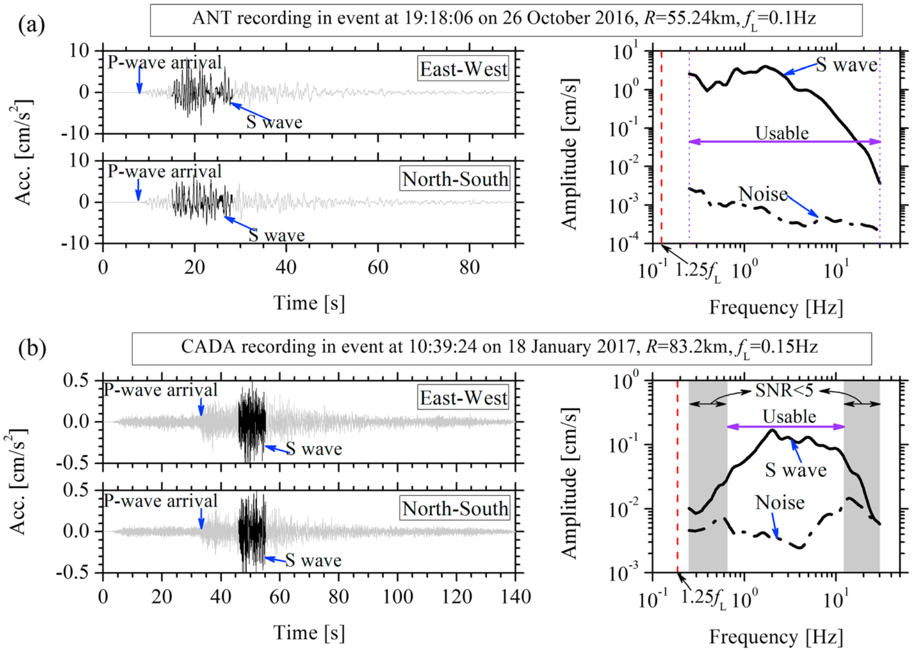

Figure 3. Examples of extracted *S* waves and calculated *S* wave and noise Fourier spectra for (a) the ANT recording of the 26 October 2016 event at 19:18:06 UTC and (b) the CADA recording of the 18 January 2017 event at 10:39:24 UTC. The usable frequency bands of the Fourier spectra for both *S* waves were identified according to both the signal-to-noise ratios (SNRs) and the low-cut corner frequencies (f_L).

ANT recording of the 26 October 2016 event at 19:18:06 UTC, whereas the usable frequency band for the CADA recording of the 18 January 2017 event at 10:39:24 UTC is limited to a narrower range of 0.65–12.24 Hz because of the strong pre–*P* wave noise at lower and higher frequencies. The numbers of usable Fourier spectra at each frequency from 0.25 to 30 Hz are shown in Figure 4a. The number of usable Fourier spectra was dependent on frequency, decreasing from >5,000 at frequencies of 1–10 Hz to about 4,000 or less at both lower and higher frequencies. At least three quarters of all Fourier spectra were available at frequencies of 0.25–30 Hz. The minimal and maximal numbers of usable Fourier spectra were 3,860 and 5,133 at 30 and 1.85–1.91 Hz, respectively. The numbers of usable spectra for each event and for each site selected are plotted against frequency from 0.25–30 Hz in Figures 4b and 4c, respectively. It can be seen that the numbers of usable spectra at frequencies of 0.25–30 Hz were not less than three for all events, except for one event that occurred on 26 October 2016 at 19:25:18 UTC, which had only one usable spectrum at frequencies below ~0.4 Hz. However, some stations had zero, one, or two usable

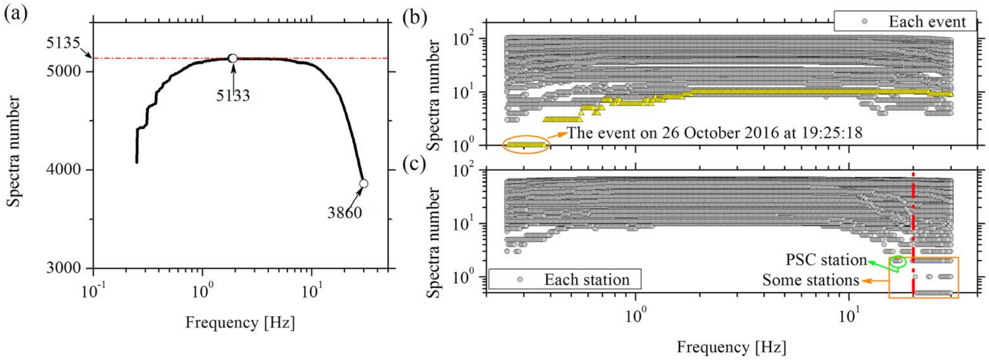

Figure 4. (a) Numbers of usable Fourier spectra at frequencies from 0.25–30 Hz. Numbers of usable Fourier spectra (b) for each event and (c) for each station considered in this study at frequencies from 0.25–30 Hz. In panel (c), the numbers of usable spectra equal to zero for a few stations are plotted on the horizontal axis.

spectra mainly at frequencies over ~20 Hz, except for station PSC, which had two usable spectra at frequencies of 16.0–17.5 Hz. The frequency band of 0.25–20 Hz was thus applied in this study to guarantee data redundancy in the spectral inversion.

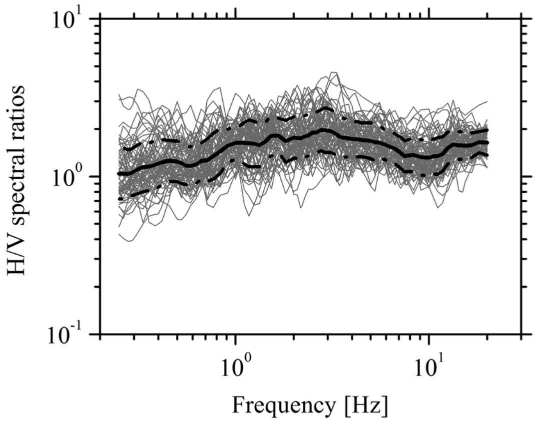

Figure 5. Calculated site responses using strong-motion data recorded at the LSS station based on the horizontal-to-vertical (H/V) spectral ratio technique (gray lines). Black solid and dashed-dotted lines represent the mean and the ±1 standard deviation, respectively.

3. Methodology

In this study, we used the two-step nonparametric GIT (Bindi et al., 2004; Castro et al., 1990) to separate simultaneously the source spectra, site response functions, and propagation path attenuation from the observed ground motions in the frequency domain. The acceleration spectral amplitude at frequency f_m can be expressed as

$$O_{ij}\left(f_m, R_{ij}\right) = M_i(f_m)A\left(f_m, R_{ij}\right), \tag{1}$$

where $O_{ij}(f_m, R_{ij})$ is the spectral amplitude observed at the jth station resulting from the ith earthquake, R_{ij} is the hypocentral distance, $M_i(f_m)$ is a scalar dependent on the size of the ith earthquake, and $A(f_m, R_{ij})$ is a nonparametric function of distance and frequency that accounts for seismic attenuation along the travel path (geometrical spreading, anelastic attenuation and scattering attenuation, refracted arrivals, etc.). $A(f_m, R_{ij})$ is not supposed to have any parametric functional form in advance, and it is constrained as a smooth function of distance with a value of 1 at the reference distance $R_0 = 6.2$ km, which is the smallest hypocentral distance for recordings considered in our study. In practice, the hypocentral distance of the usable spectra at frequency f_m was divided into $N_{D,m}$ bins with 1-km width, and $A(f_m, R_{k,m})$ instead of $A(f_m, R_{ij})$ was computed, where $R_{k,m}$ represents the average hypocentral distance of the usable spectra at frequency f_m lying within the kth distance bin. After linearization by taking the logarithm, equation (1) can be solved easily using the singular value decomposition (SVD) method.

Once $A(f_m, R_{k,m})$ is determined, the spectral amplitudes can be corrected for seismic attenuation. The path-corrected spectra are divided into source spectra and site response functions:

$$O_{ij}\left(f_m, R_{ij}\right)/A(f_m, R_{k,m}) = S_i(f_m)G_j(f_m), \tag{2}$$

where $G_j(f_m)$ is the site response function at the jth station and $S_i(f_m)$ is the source spectrum of the ith earthquake. To remove the trade-offs between source and site effects, one or more reference sites with available site responses or reference events with determined source spectra should be fixed beforehand for the solution of equation (2). In this study, the rock station Leonessa (LSS), classified as a class A site in Eurocode 8 with $V_{S30} = 1091$ m/s, was selected as the reference site. This station was also selected by Bindi et al. (2009) as one of two reference sites, with constant site response at frequencies of 0.3–20 Hz, for spectral inversion analysis of the 2009 L'Aquila seismic sequence. As reported by Atkinson and Cassidy (2000), Siddiqqi and Atkinson (2002), and Atkinson (2004), the observed amplifications for rock sites were approximately consistent with the horizontal-to-vertical (H/V) spectral ratios of the body waves. Bindi et al. (2004) constrained the site response at reference station ASSI as the H/V spectral ratios for the spectral inversion. Hence, the H/V spectral ratios of the 73 strong-motion data recorded at the LSS station during 2009–2017, with maximum PGA of ~50 cm/s^2, were calculated at frequencies of 0.25–20 Hz (as shown in Figure 5), and the average spectral ratio (black solid line in Figure 5) was used as the site response. The SVD method was also adopted to solve equation (2) for the source spectra and the site response functions.

4. Path Attenuation

Path attenuation curves versus hypocentral distances at frequencies of 0.25–20 Hz were derived from the solution of equation (1), and they are plotted in Figure 6a. In principle, path attenuation curves are between $R^{-0.5}$ and R^{-1} at near-source distances (i.e., <10 km) but between R^{-1} and R^{-2} at distances of 20–100 km. Path attenuation curves decline continuously with the increasing distance for all frequencies at distances ≤60 km; however, they show large variations with different frequencies at distances >60 km. Although they become gradually flat at low frequencies (i.e., approximately ≤1.0 Hz), they exhibit much faster decay at

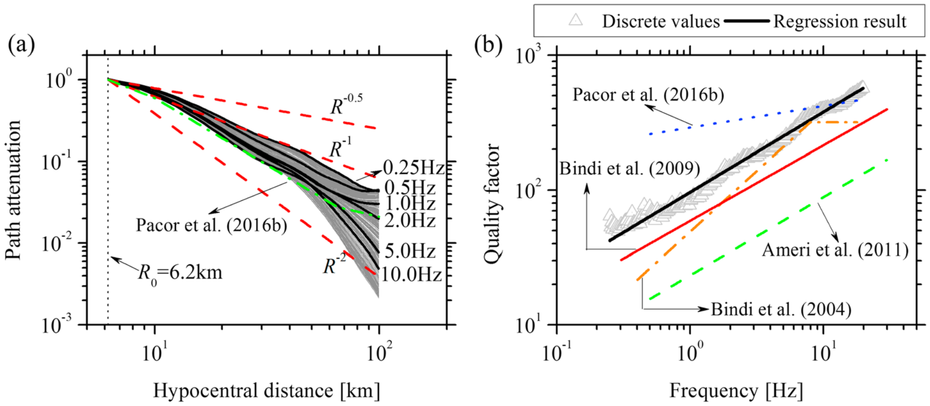

Figure 6. (a) Nonparametric path attenuation curves at frequencies of 0.25–20 Hz (gray lines). Attenuation curves at some typical frequencies (i.e., 0.25, 0.5, 1.0, 2.0, 5.0, and 10.0 Hz) are highlighted by dark lines. Geometrical spreading represented by R^{-n} with n values equal to 0.5, 1, and 2 is also plotted (dashed lines). The geometrical spreading model established by Pacor, Spallarossa, et al. (2016) for the 2009 L'Aquila seismogenic region is plotted using the dashed-dotted line. (b) Calculated Q values (triangles) and optimal least squares fitting according to the functional form of $Q = Q_0 f^{\eta}$. The Q models of other studies with respect to central Italy are also plotted, that is, Bindi et al. (2009), Ameri et al. (2011), and Pacor, Spallarossa, et al. (2016) for the 2009 L'Aquila seismogenic region and Bindi et al. (2004) for the 1997 Umbria-Marche seismogenic region.

high frequencies (i.e., approximately >5.0 Hz). The decay changes at distance beyond 60 km might reflect reverberations from the Moho in the study region.

It is desirable to represent path attenuation using the parametric formulation in equation (3), which accounts for geometrical spreading and anelastic attenuation:

$$\ln\left[A\left(f_m, R_{k,m}\right)\right] = n\ln\left(\frac{R_{0m}}{R_{k,m}}\right) + \frac{f_m}{Q\left(f_m\right)}\left[\frac{-\pi\left(R_{k,m} - R_{0m}\right)}{\beta}\right], \quad (3)$$

where β is the shear-wave velocity set to 3.15 km/s at depths of 7.5–14.5 km, according to the central Italian Apennines velocity model used by Herrmann et al. (2011), $Q(f_m)$ stands for the S wave quality factor at frequency f_m constraining the anelastic attenuation, and n is the geometrical spreading exponent.

We assumed n independent of frequency and hypocentral distance, and we ignored the potential azimuth dependence of Q (Pavel & Vacareanu, 2018); thus, equation (3) was solved for the optimum n and frequency-dependent Q values using the SVD method. The calculated value of n is equal to 1.0 in this study, which is similar to the constant n value (~0.9) at frequencies of 0.5–20 Hz in the 1997 Umbria-Marche seismogenic region reported by Bindi et al. (2004). However, both Pacor, Spallarossa, et al. (2016) and Bindi et al. (2017) used a trilinear piecewise function of the hypocentral distance to achieve a parameterized description of the geometrical spreading for the 2009 L'Aquila seismogenic region. Both studies considered the similar hypocentral distance ranges, ~5–120 km, to our study (~6–100 km). They obtained similar geometrical spreading models, and the model established by Pacor, Spallarossa, et al. (2016) is plotted in Figure 6a for comparison with the path attenuation derived in our study. It can be seen that the geometrical spreading in the L'Aquila seismogenic region with hypocentral distances less than ~40 km is stronger than the weaker path attenuation in our study region. More obviously, much weaker geometrical spreading was revealed in the 2016–2017 seismogenic region compared with the L'Aquila region.

The calculated Q values at frequencies of 0.25–20 Hz are plotted in Figure 6b. The Q values usually increase monotonically as a function of frequency in the form $Q(f) = Q_0 f^{\eta}$, where Q_0 indicates the Q value at 1 Hz and η is the frequency-dependent coefficient. The values of $Q_0 = 96.56$ and $\eta = 0.58$ were provided based on a power-function regression. The optimal least squares fitting models from the inverted Q values using the L'Aquila sequence (Ameri et al., 2011; Bindi et al., 2009; Pacor, Spallarossa, et al., 2016) and the Umbria-Marche sequence (Bindi et al., 2004) are also plotted in Figure 6b. Although similar L'Aquila seismogenic regions were considered, significantly different Q models were reported by several studies due to the different hypocentral distance ranges considered, 5–50 km by Bindi et al. (2009), 8–30 km by Ameri et al. (2011),

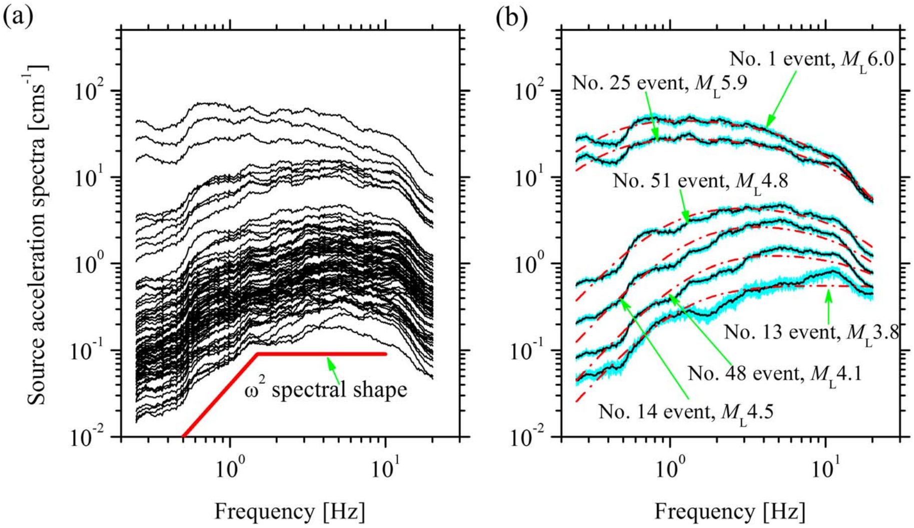

Figure 7. (a) Inverted source acceleration spectra for events considered in this study. (b) Best fitting theoretical spectra to the inverted spectra for six typical events represented by earthquake numbers, as shown in Table S1 in the supporting information. In order to reflect the stability of the inverted source spectra, source spectra from 100 bootstrap inversions were plotted in cyan lines.

and 5–120 km by Pacor, Spallarossa, et al. (2016). The Q values estimated in our study are close to the results of Bindi et al. (2009) for the L'Aquila region and of Bindi et al. (2004) for the Umbria-Marche region. However, our findings are significantly higher than the results of Ameri et al. (2011) and lower than the results of Pacor, Spallarossa, et al. (2016) at low–moderate frequencies (i.e., 0.4–7 Hz).

5. Earthquake Self-Similar Scaling

The inverted source acceleration spectra for the considered events are shown in Figure 7a. We first performed the bootstrap analysis to assess the stability of the inverted source spectra. Approximately 15% of the usable spectral at each frequency were removed randomly from the data set, and the remaining ones were assembled as a new data set used in the bootstrap inversion. The source spectra were calculated from repeated procedures in 100 bootstrap inversions to investigate the stability of source spectra. Figure 7b shows the source spectra from 100 bootstrap inversions for six typical events, compared with the inverted source spectra using the whole data set. It was found that the deviation of source spectra in bootstrap inversions from the source spectra obtained using the whole data set remains small, implying that the source spectra are stable.

In general, the spectral shapes match well the well-known ω-square source model (Brune, 1970), except at high frequencies (>~10 Hz). However, it is striking that rapid decay universally appears in the high-frequency spectra. This could be ascribed to the high-frequency κ decay, usually expressed in the form $\exp(-\pi f\kappa)$, which is ultimately interpreted as the superposition of the effects of S wave attenuation through the subsurface geological structure and the distance-dependent attenuation due to horizontal propagation of seismic waves within the crust (Anderson & Hough, 1984; Campbell, 2009; Ktenidou et al., 2013). Controversially, Kilb et al. (2012) suggested distance-dependent κ attenuation might be included in the path attenuation term or might not actually exist. The high-frequency κ decay that really exists at the reference site but not considered might move into the source spectra, as has been observed by some other studies, for example, Oth et al. (2011) and Oth and Kaiser (2014). Thus, our study considered high-frequency κ decay in the inverted source spectrum, which describes the mean effects over all stations recorded during this event. The inverted source spectrum can be expressed theoretically as

$$S(f) = (2\pi f)^2 \frac{R_{\Theta\Phi} VF}{4\pi\rho\beta^3 R_0} \frac{M_0}{1+(f/f_c)^2} \exp(-\pi f\kappa). \tag{4}$$

where M_0 and f_c are the seismic moment and corner frequency, respectively. Here $R_{\Theta\Phi}$ is set to 0.55 to account for the average radiation pattern over a suitable range of azimuths and take-off angles (Boore & Boatwright, 1984), $V = 1/\sqrt{2}$ represents the partitioning of the total S wave energy into horizontal components, $F = 2$ is the free surface factor, ρ is the density in the vicinity of the source (set to 2.6 g/cm^3 according to the central Italian Apennines model in Herrmann et al., 2011), and reference distance R_0 is 6.2 km. We applied a grid-searching technique to retrieve the optimum parameters of M_0, f_c, and κ for individual events. The estimations are listed in Table S1 in the supporting information. The relationship between the moment magnitude M_w and M_0 proposed by Hanks and Kanamori (1979) was used for the calculation of M_w. The parameters were expected to provide the theoretical spectrum, expressed as in equation (4), closest to the inverted spectrum covering the entire frequency band of 0.25–20 Hz. As shown in Figure 7b for six typical events, the theoretical and inverted spectra are mostly in good agreement.

Moreover, we verified the reliability of the grid-searching technique for estimating the source parameters (i.e., M_w and f_c) from the inverted spectra. For this purpose, a series of prior spectra (a total of 352) characterized by prior combination of M_w, f_c, and κ values were constructed based on equation (4), where $M_w = 3.75$, 4.25, 5, and 6; $f_c = 0.3$, 0.5, 0.8, 1.0, 1.5, 2.0, 3.0, and 4.0 Hz; and $\kappa = 0$–0.05 s at a constant interval of 0.005 s. Then, the residuals between the inverted and the best fitted theoretical spectra from six typical events (plotted in Figure 7b) were considered to modify the smooth prior spectra. Finally, we constructed a total of 2,112 prior spectra. The grid-searching technique was applied to obtain the optimum M_w, f_c, and κ values for individual prior spectra. The deviations of the optimum to prior M_w values against the prior f_c values were shown in Figure S1 in the supporting information. The deviations between the optimum and prior M_w values are generally less than 0.1 magnitude units when the prior f_c values are equal to or greater than 0.5 Hz. In our study, 75 out of the 78 events were estimated as $f_c > 0.5$ Hz (Table S1 in the supporting information), indicating the reliable estimations of the M_w values. The remaining three major events with $M_L \sim 6.0$ were estimated as $f_c = {\sim}0.3$ Hz. However, the M_w values estimated for two events with $M_L = 6.0$ and 5.9 show remarkable consistency to the time domain moment tensor solutions of INGV. The optimum f_c values against the prior values for each prior κ value are shown in Figure S2 in the supporting information. Although good consistencies between the estimated and prior f_c values are observed when the prior f_c values of 0.5–2.0 Hz are assigned irrespective of the value of κ, the estimated f_c values show large deviations to the prior values when the smaller and larger prior f_c values (<0.5 and >2.0 Hz) are assigned. In our study, most events were estimated as $f_c = 0.5$–2.0 Hz, implying the reliable f_c estimations for these events. However, three major events with $M_L \sim 6.0$ were estimated as $f_c = {\sim}0.3$ Hz, and two smaller events were estimated as $f_c > 2.0$ Hz (Table S1 in the supporting information). It is debatable whether the f_c estimations for the five events using the grid-searching technique are reliable or not. In general, the grid-searching technique was acceptable for the estimations of M_w and f_c values from the inverted source spectra.

Earthquake self-similar scaling is a controversial issue characterized by a constant stress drop ($\Delta\sigma$) over a wide range of earthquake sizes. It was originally recognized by Aki (1967), and it has been observed in large numbers of earthquakes, for example, global moderate–large earthquakes (Allmann & Shearer, 2009), Japanese crustal or subcrustal earthquakes (Oth, 2013), and the 2008 Wenchuan seismic sequence (Wang et al., 2018). However, the breakdown of earthquake self-similar scaling has been verified in certain specific seismic sequences, for example, the 2004 Les Saintes Guadeloupe seismic sequence (Drouet et al., 2011) and the 2009 L'Aquila seismic sequence (Pacor, Spallarossa, et al., 2016). The question of whether self-similar scaling was followed during the 2016–2017 central Italy seismic sequence was investigated in our study. According to an expanding circular crack, the stress drop can be calculated based on estimations of M_0 and f_c using the following relation (Brune, 1970):

$$\Delta\sigma = \frac{7M_0}{16}\left(\frac{2\pi f_c}{2.34\beta}\right)^3. \tag{5}$$

The calculated $\Delta\sigma$ values for this seismic sequence, listed in Table S1 in the supporting information, fall within a wide range from 0.113 to 12.190 MPa. Our estimates for this sequence are generally lower than those previously observed in central Italy: 0.2–25.0 MPa for the 2009 L'Aquila seismic sequence with $M_L = 3.0$–5.9 (Ameri et al., 2011; Pacor, Spallarossa, et al., 2016), an average of ~2 MPa for the Umbria-Marche seismic sequence with $M_L = 1.4$–5.9 (Bindi et al., 2001, 2004), and approximately 0.3–30.0 MPa for a large number of events of $M_L = 3$–6 during 2008–2013 in central Italy (Bindi et al., 2017). The $\Delta\sigma$ values

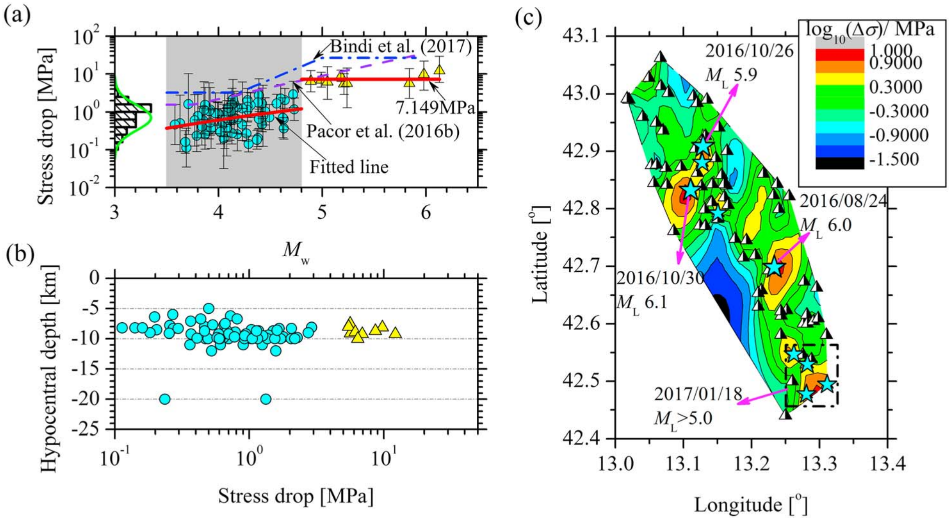

Figure 8. (a) Stress drop values versus moment magnitudes (M_W). The error bars indicate ±1 standard deviation. The histogram depicts the lognormal distribution of $\Delta\sigma$ values for events of $M_W < 4.80$. Solid lines represent the linear best fit between $\Delta\sigma$ and M_W for $M_W < 4.80$ and $M_W > 4.80$. The $\Delta\sigma$-M_W relationships established by Pacor, Spallarossa, et al. (2016) and by Bindi et al. (2017) are compared. (b) Stress drop values versus hypocentral depths. (c) Spatial distribution of $\Delta\sigma$ values for events considered in this study. Stars indicate moderate events of $M_L > 5.0$ (i.e., $M_W > 4.80$); triangles represent small events of $M_L < 5.0$ (i.e., $M_W < 4.80$).

for 69 events of $M_L < 5.0$ (i.e., $M_W = 3.58$–4.73), in the range from 0.113 to 2.905 MPa, show an approximate trend of slow increase with increasing M_W, which can be described approximately by a lognormal distribution with a mean of 0.709 MPa and a standard deviation of 0.333 on the base-10 logarithmic scale. However, the $\Delta\sigma$ values for the remaining nine events with $M_L > 5.0$ (i.e., $M_W = 4.89$–6.13), in a narrow range from 5.475 to 12.190 MPa with a mean of 7.149 MPa and a standard deviation of 0.123 on the base-10 logarithmic scale, exhibit small variation with M_W value. The mainshock on 24 August (No. 1) and two subsequent major events on 26 and 30 October (Nos. 25 and 35) resulted in large stress drops of 9.775, 5.618, and 12.190 MPa, respectively. The finding that $\Delta\sigma$ values present high variability for events with smaller magnitude ($M_L < 5.0$) compared with the larger ones observed in the 2016–2017 sequence has been confirmed in many previous studies (e.g., Allmann & Shearer, 2009; Oth et al., 2010). This could indicate that small earthquakes are likely to propagate in a rough fluctuating stress field, while large earthquakes propagate across a relatively smooth correlated field, as argued by Ben-Zion and Zhu (2002) and Ben-Zion et al. (2003). During earthquake failure, the slip increases with rupture dimension considerably less in a strongly heterogeneous stress field than it does in a relatively homogenous stress field (Ben-Zion, 2008; Fisher et al., 1997). Since the stress drop on a given rupture area correlates with the amount of slip, this might explain the increasing stress drops with the event size.

The magnitude-dependent $\Delta\sigma$ values, seen clearly in the plots of $\Delta\sigma$ against M_W in Figure 8a, indicate a breakdown of earthquake self-similar scaling in this seismic sequence over the range of $M_W = 3.58$–6.13. Moreover, a parameter ε in the formula $M_0 \propto f_c^{-(3+\varepsilon)}$ proposed by Kanamori and Rivera (2004) was calculated to evaluate quantitatively the deviations from self-similarity. In the case of $\varepsilon = 0$, self-similarity is followed perfectly, while the case of $\varepsilon > 0$ ($\varepsilon < 0$) indicates an increasing stress drop with increasing (decreasing) magnitude. In this study, a value of $\varepsilon = 0.36 \pm 0.29$ was determined from the regression analysis, implying a breakdown of earthquake self-similar scaling in this seismic sequence. In central Italy, a breakdown of earthquake self-similar scaling also occurred in the L'Aquila seismic sequence (Bindi et al., 2017; Pacor, Spallarossa, et al., 2016), whereas self-similar scaling was followed by the Umbria-Marche seismic sequence over the range of $M_L = 1.4$–5.9 (Bindi et al., 2004, 2001). The regressed magnitude-dependent $\Delta\sigma$ models based on the L'Aquila events with hypocentral depths of 6–10 km (Pacor, Spallarossa, et al., 2016) and with hypocentral depths deeper than 8 km (Bindi et al., 2017) are plotted in Figure 8a for comparison with the $\Delta\sigma$-M_W plots of our study. The M_W-independent model for $M_W > 5.0$, proposed by Bindi et al. (2017), is scaled to the $\Delta\sigma$-M_W plots of our study, although their model reveals larger $\Delta\sigma$ values. Both models also exhibit a trend of increase of $\Delta\sigma$ with M_w when $M_\mathrm{w} = 4.2$–5.0 (Bindi et al., 2017) and when $M_\mathrm{w} > 3.9$ (Pacor, Spallarossa, et al., 2016).

Previous studies have confirmed that $\Delta\sigma$ values are also dependent on hypocentral depth, for example, the L'Aquila seismic sequence (Bindi et al., 2017; Pacor, Spallarossa, et al., 2016) and Japanese earthquakes (Oth, 2013). In general, deeper events appear to cause large stress release. Figure 8b shows plots of $\Delta\sigma$ against hypocentral depth for the 2016–2017 central Italy sequence. The independence between $\Delta\sigma$ and hypocentral depth can be seen clearly over the range of hypocentral depth from ~5 to ~12 km. The $\Delta\sigma$ values for two events with deep hypocentral depths (~20 km) do not show any significant discrepancy with other events of similar magnitude but shallower hypocentral depth. Moreover, lateral inhomogeneity of the strength of the subsurface geological material might also cause the variation of the $\Delta\sigma$ values. Figure 8c shows the spatial distribution on the horizontal projection plane of the $\Delta\sigma$ values on the base-10 logarithmic scale as obtained from assembling and interpolating $\Delta\sigma$ values for the 76 events considered in this study (except the two events with relatively deeper hypocentral depth in comparison with the others) by the tension spline interpolation method. The high-$\Delta\sigma$ patches, which mainly nucleate around the 24 August M_L 6.0 mainshock (south central section), the two major events on 26 and 30 October (north central section), and four $M_\mathrm{L} > 5.0$ aftershocks on 18 January (southernmost section), are scattered within the epicentral area. Apart from the high-$\Delta\sigma$ patches, other $\Delta\sigma$ values are plotted at lower levels. The depth-independence and scattered spatial distribution within the epicentral area for events with high $\Delta\sigma$ values further confirmed the fact that the $\Delta\sigma$ values are dependent on the M_w value (i.e., the breakdown of earthquake self-similar scaling).

The 2016–2017 central Italy seismic sequence can be characterized by the occurrence of multiple major earthquakes on the local fault systems within a short period. Before this sequence, seismic sequences with multiple major shocks have been observed frequently in central Italy (e.g., the 1997 Umbria-Marche and 2009 L'Aquila sequences). After the initial mainshock (i.e., the 24 August M_L 6.0 event) that released high stress drops on the southern portion of the Mt. Vettore-Mt. Bove fault system and on the northern portion of the Laga Mts. fault system (Figure 1), the small aftershocks that occurred immediately afterward around the area of the mainshock released low stress drops. However, 2 months later, the 26 October M_L 5.4 and M_L 5.9 and 30 October M_L 6.1 events again released high stress drops on the northern portion of the Mt. Vettore-Mt. Bove fault system. The four $M_\mathrm{L} > 5.0$ events on 18 January 2017 that occurred to the south of the mainshock produced the final high stress releases in this sequence. The other small aftershocks that occurred intermittently during that time generally showed low stress drops. Kenner and Simons (2005) proposed that earthquakes with high stress drops are likely to induce successive occurrence of multiple major earthquakes resulting from postseismic stress transfer. Similarly, Chen et al. (2013) also verified that high-stress changes from neighboring events cause significant reduction of recurrence intervals. We thus inferred that intensive stress release of the mainshock and lower stress release during subsequent smaller events might cause rapid accumulation of stress on extensional unruptured faults activated in the mainshock, which might be one reason for the occurrence of the subsequent major events. Based on inverted kinematic source models for the three largest earthquakes in this sequence, Chiaraluce et al. (2017) suggested the occurrence of subsequent major events later in the sequence and, in part, the rupturing of an already activated fault plane might have been due to complex effects of the perturbation of stress loads on the volume containing the fault plane.

6. Source Rupture Directivity

Source rupture directivity, the manner in which an earthquake rupture propagates asymmetrically across an extensional fault in time and space, is prone to occur not only in most large earthquakes (McGuire et al., 2002) but also in many small–moderate earthquakes (Kane et al., 2013; Tan & Helmberger, 2010; Wen et al., 2015). It has been generally recognized that source rupture directivity leads to strong azimuthal dependence both in the duration of the apparent source time function and in the spectral amplitude of the apparent source spectrum, which are termed rupture directivity effects. Source rupture directivity effects are usually expressed in the simple form of ${C_\mathrm{d}}^{\gamma}$ as a function of the orientation of the fault relative to the station and the direction and velocity of rupture propagation. The rupture directivity coefficient C_d was originally introduced by Ben-Menahem (1961) for completely unilateral rupture propagation and then improved by Boatwright (2007) for asymmetrical bilateral rupture propagation under an assumption of a homogeneous kinematic line source model. Following Boatwright (2007), C_d can be expressed as

$$C_{\mathrm{d}} = \sqrt{\frac{k^2}{\left[1-\left(\frac{v_{\mathrm{r}}}{\beta}\right)\cos\vartheta\right]^2} + \frac{(1-k)^2}{\left[1+\left(\frac{v_{\mathrm{r}}}{\beta}\right)\cos\vartheta\right]^2}}, \tag{6}$$

where v_{r}/β is the Mach number (where v_{r} is the rupture velocity) and ϑ is the angle between the ray that leaves the source and the direction of rupture propagation (Joyner, 1991), which can be expressed simply as the difference between the horizontal rupture direction φ and the station azimuth. Here parameter k represents the relative portion of rupture length in the direction φ accounting for the entire rupture length. It is an index to determine whether φ is the predominant horizontal rupture direction. Effectively, a value of $k > 0.5$ reveals that the retrieved φ is the predominant direction; otherwise, the opposite direction (i.e., $\varphi + 180°$ if $\varphi < 180°$ or $\varphi - 180°$ if $\varphi \geq 180°$) is predominant. In this study, the rupture parameters v_{r}/β, φ, and k in equation (6) were estimated to describe source rupture directivity.

The exponent γ in the form of ${C_{\mathrm{d}}}^{\gamma}$ is dependent on the source model considered. For source models with heterogeneous distributions of slip and rise time or with incoherent rupture propagation, the value of γ decreases from 2 or 1 (for models with constant slip and rise time) to 0 (for purely stochastic and composite models). However, ambiguity remains regarding the determination of the optimal value of γ to reflect source rupture directivity (Ruiz et al., 2011). In practical applications, $\gamma = 1$ (Bernard et al., 1996; Boatwright, 2007; Wen et al., 2015) and $\gamma = 0.5$ (Gallovič, 2016; Ren, Wang, & Wen, 2017) have been validated in explanations of the directivity effects on either observed ground motions or apparent source spectra produced by asymmetrical source rupture. Gallovič (2016) showed the best fit with observed strong-motion data near a fault for frequencies >1 Hz is provided by a model with $\gamma = 0.5$. Meanwhile, Ren, Wang, and Wen (2017) discussed the strong influence of uncertainty regarding γ on the estimation of v_{r}/β and k, and they proposed that a model with $\gamma = 0.5$ produces reliable estimations of v_{r}/β.

Our study selected 36 of 78 events (marked in Table S1 in the supporting information) to investigate their potential source rupture directivity through analysis of the azimuthal dependence in the apparent source spectra. To achieve reasonable spatial coverage, we stipulated that each selected event should be recorded by at least 60 strong-motion stations, of which the site response functions were obtained in this study, and that more than five stations should be available in each quadrant of a Cartesian coordinate system taking the epicenter as the origin. The apparent source spectra (S_{a}) at each station were obtained after removing path attenuation terms and site responses from the observed S wave Fourier spectra considered in this study according to equation (2). The residuals, that is, the differences between the apparent source spectra and the event mean source spectrum (i.e., the inverted source spectrum in this study) on the base-10 logarithmic scale, were calculated at frequencies of 0.25–20 Hz to reflect the azimuthal variation of the apparent source spectra. Plots of residuals against azimuth at six frequencies (0.5, 1.0, 2.0, 5.0, 8.0, and 12.0 Hz) are shown separately in Figure 9 for two typical events (the M_{L} 6.0 mainshock [No. 1] and an M_{L} 4.0 event on 30 October 2016 at 11:58:17 UTC [No. 42]) and in Figure S3 in the supporting information for the remaining 34 events. The residuals at partial frequencies for some events exhibit significant variations with azimuth, whereas no obvious azimuthal variation at most of the six frequencies is also observed in relation to other events. One or two peaks occur in the residuals with significant azimuthal variation (rather than four peaks due to the radiation pattern), implying source rupture directivity makes the primary contribution to the strong azimuthal variation of the residuals.

We applied the $\log_{10}({C_{\mathrm{d}}}^{\gamma})$ curve to fit the azimuthal residuals at each of the 20 frequencies selected over the range from 0.3 to 15.0 Hz for each event, according to the least squares method, and we expected to retrieve optimal values of the rupture parameters, that is, v_{r}/β, φ, and k. The γ values were set separately to 0.5, 0.75, 1, and 2 in this study to illustrate the effects of γ uncertainty on the retrieved rupture parameters. The best fitted $\log_{10}({C_{\mathrm{d}}}^{\gamma})$ curves are included in residual plots at the six frequencies, as shown in Figures 9 and S3 in the supporting information. Moreover, the average deviations between the best fitted $\log_{10}({C_{\mathrm{d}}}^{\gamma})$ values and the residuals are also provided at the 20 frequencies selected. In principle, reasonable agreement between the best fitted $\log_{10}({C_{\mathrm{d}}}^{\gamma})$ curves and the azimuthal residuals was observed for most events, irrespective of the value of γ selected. However, for some events, for example, Nos. 20 and 57 (see Figure S3 in the supporting information), we noted the best fitted $\log_{10}({C_{\mathrm{d}}}^{\gamma})$ curves were unable to represent the extremely large negative residuals, indicating intensive azimuthal variation of the apparent source spectra. Compared

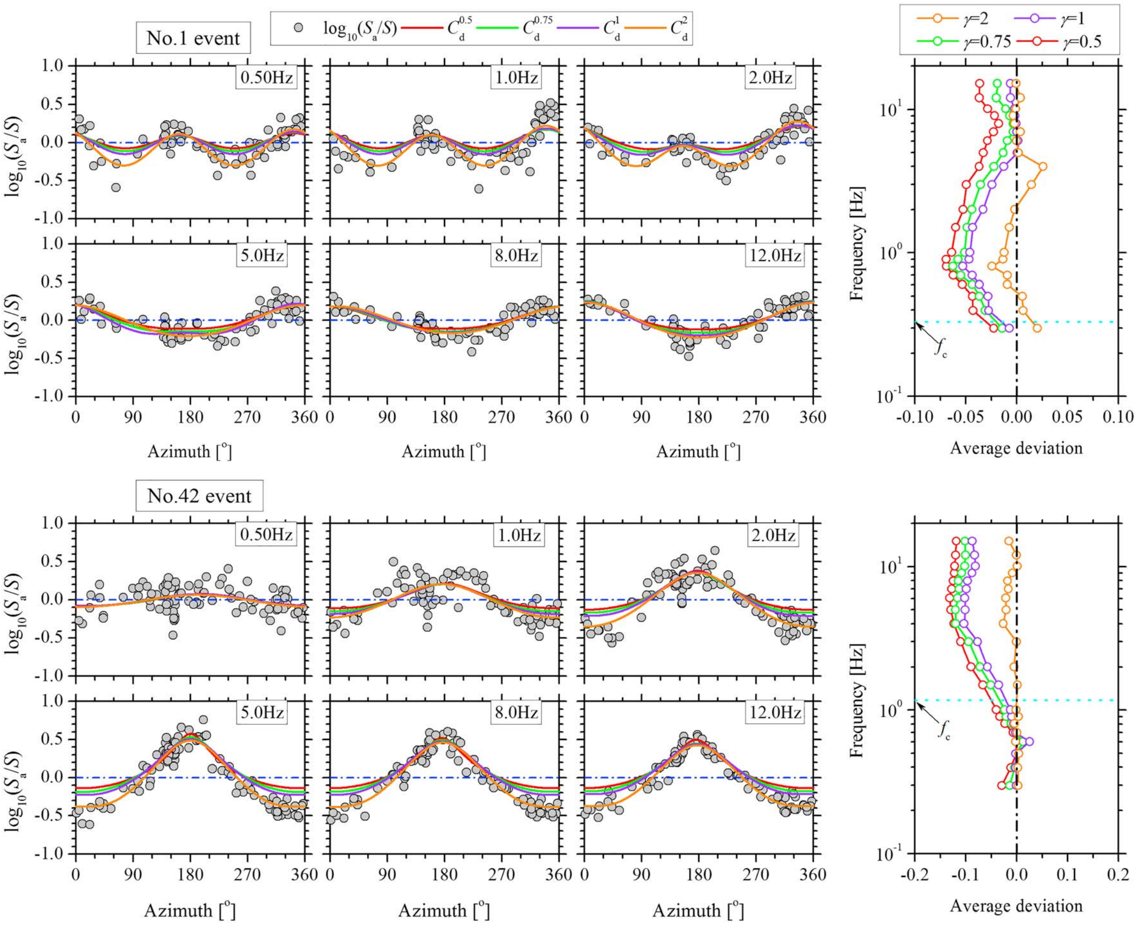

Figure 9. Residuals between apparent source spectra (S_a) and mean source spectrum (S) inverted in this study on the base-10 logarithmic scale plotted against azimuth at frequencies of 0.5, 1.0, 2.0, 5.0, 8.0, and 12.0 Hz for event nos. 1 and 42. Events corresponding to earthquake numbers are shown in Table S1 in the supporting information. The $\log_{10}(C_d{}^{\gamma})$ curves with $\gamma = 0.5$, 0.75, 1, and 2 were used to fit the azimuthal residuals. Average deviations between the best fitted $\log_{10}(C_d{}^{\gamma})$ values and the residuals are provided at the 20 frequencies selected.

with the best fitted $\log_{10}(C_d{}^{\gamma})$ curves with γ values of 0.5, 0.75, and 1, the curves for the case of $\gamma = 2$ are better qualified to represent the relatively large negative residuals, and thus, they result in smaller average deviation, for example, the residuals at frequencies of 0.5, 1.0, and 2.0 Hz and at 5.0, 8.0, and 12.0 Hz for the No. 1 event and the No. 42 event, respectively (Figure 9). We also noted that when representing the significant variation of the residuals with azimuth, the best fitted $\log_{10}(C_d{}^{\gamma})$ curves show remarkable consistency between the different γ values selected. However, the curves exhibit visible discrepancies in the case of weak azimuthal variation of the residuals (e.g., residuals at frequency of 2.0 Hz for the No. 5 event in Figure S3 in the supporting information); nevertheless, they are all qualified to match the azimuthal residuals well and they result in small average deviations.

The retrieved v_r/β results (720 values at 20 frequencies for 36 selected events) versus the ratios of the maximal and minimal $C_d{}^{\gamma}$ values over the azimuth range of 0°–360° (hereafter, denoted Max.$C_d{}^{\gamma}$/Min.$C_d{}^{\gamma}$), according to the results of v_r/β, φ, and k for the cases of γ = 0.5, 0.75, 1, and 2, are plotted in Figure 10a. The value of Max.$C_d{}^{\gamma}$/Min.$C_d{}^{\gamma}$ was used to represent quantitatively the significance of the azimuthal variation of the residuals. Larger values of Max.$C_d{}^{\gamma}$/Min.$C_d{}^{\gamma}$ indicate greater significance of the azimuthal variation of the residuals. As shown in Figure 10a, the v_r/β values generally show a pronounced trend of decrease with increasing γ, indicating the vital impact of γ on the retrieved v_r/β parameters, which has been widely verified (Pacor, Gallovič, et al., 2016; Ren, Wang, & Wen, 2017). In addition, larger v_r/β values appear to result in the larger values of Max.$C_d{}^{\gamma}$/Min.$C_d{}^{\gamma}$, that is, more significant azimuthal variation of the residuals. We further computed the proportion of the number of v_r/β

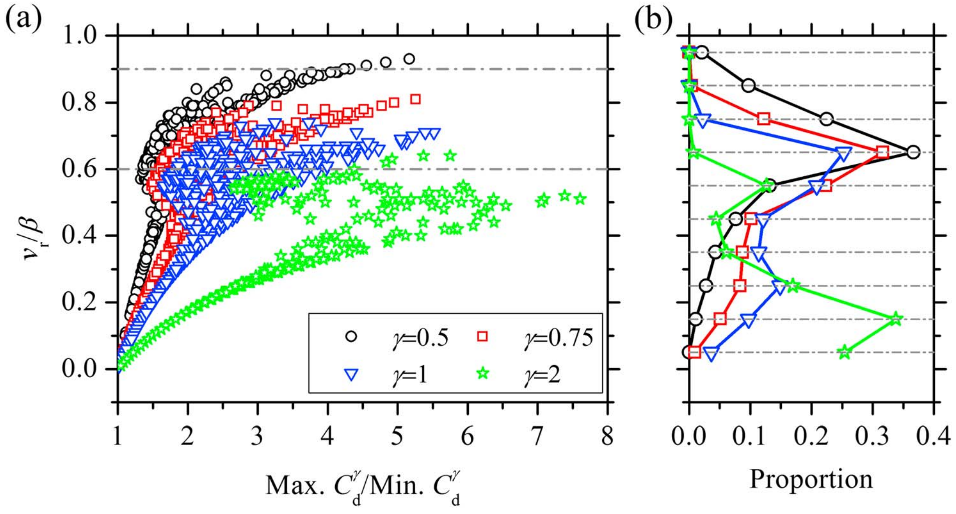

Figure 10. (a) Retrieved v_r/β values versus the ratios between the maximal and minimal $C_d{}^\gamma$ values over the azimuth range of 0°–360° (denoted by Max.$C_d{}^\gamma$/Min.$C_d{}^\gamma$) for cases of $\gamma = 0.5$, 0.75, 1, and 2, respectively. (b) Proportion of the number of retrieved v_r/β values in each bin with a width of $v_r/\beta = 0.1$ in relation to the total number (i.e., 720) of retrieved v_r/β values for cases of $\gamma = 0.5$, 0.75, 1, and 2.

values in each v_r/β bin (with a width of 0.1) in relation to the total number (i.e., 720) of the retrieved v_r/β values for the cases of $\gamma = 0.5$, 0.75, 1, and 2, as shown in Figure 10b. For the case of $\gamma = 2$, none of the values of v_r/β is >0.70, very few are in the range 0.60–0.70 (<1%), and most (~75%) are in the range <0.30. For the cases of $\gamma = 0.5$, 0.75, and 1, most of the retrieved v_r/β values fall within the range 0.60–0.70, and gradually decreasing numbers of v_r/β values are observed when the v_r/β values decrease from 0.60 to 0.01 (the minimal v_r/β value limited in the least squares analysis) or increase from 0.70 to 1.00. As the γ values decrease from 1 to 0.5, the proportion of the number of v_r/β values in each bin shows an upward tendency when v_r/β is >0.60. Conversely, a downward tendency is clearly observed in those bins when v_r/β is <0.60. The total proportions of the number of $v_r/\beta > 0.60$ are 0.71, 0.44, and 0.28 for the cases of $\gamma = 0.5$, 0.75, and 1, respectively. In our study, slow-velocity rupture scenarios (i.e., small values of v_r/β) were mostly identified irrespective of the value of γ selected. In some previous studies, rupture velocity was also identified with much slower values, for example, $v_r/\beta = 0.17$–0.35 (Boatwright, 2007) and $v_r/\beta < 0.5$ for the case of $\gamma = 1$ (Pacor, Gallovič, et al., 2016) and $v_r/\beta = 0.35$–0.45 for the case of $\gamma = 2$ (Ren, Wang, & Wen, 2017). However, in view of the v_r/β values (0.6–0.9) commonly used by the seismology community, we were inclined to apply the form of $C_d{}^\gamma$ with $\gamma = 0.5$ to analyze the azimuthal residuals. Hereafter, the retrieved rupture parameters and rupture directivity for the case of $\gamma = 0.5$ only are discussed.

The values of Max.$C_d{}^{0.5}$/Min.$C_d{}^{0.5}$ at the 20 frequencies selected for each event are shown in Figure S4 in the supporting information. We found the majority of events (~26 out of the 36 events considered) show very small Max.$C_d{}^{0.5}$/Min.$C_d{}^{0.5}$ values (<2.5) at most frequencies considered, which indicates weak or absent rupture directivity effects resulting from either the much slower rupture ($v_r/\beta < 0.60$) or the approximately symmetrical bilateral rupture propagation ($k < 0.70$), as shown in Figure 11. However, 14 v_r/β-k plots from eight events (Nos. 16, 25, 44, 48, 53, 61, 69, and 71) at few frequencies (as shown in Figure S4) fall into the zones characterized by Max.$C_d{}^{0.5}$/Min.$C_d{}^{0.5} > 2.5$. Overall, 10 events (Nos. 5, 9, 20, 32, 34, 42, 49, 56, 57, and 58) have wide frequency bands including at least four continuous frequencies with Max.$C_d{}^{0.5}$/Min.$C_d{}^{0.5} \geq 2.5$ (highlighted in Figure S4), reflecting strong azimuthal variation of the residuals, which is potentially caused by strong rupture directivity. Hereafter, the corresponding frequency band is called the directivity frequency band. Details of the 10 most directive events and their directivity frequency bands with Max.$C_d{}^{0.5}$/Min.$C_d{}^{0.5} \geq 2.5$ are listed in Table 1. Except for the No. 5 event, the directivity frequency bands are all beyond the source corner frequency. Reasonably, small values of Max.$C_d{}^{0.5}$/Min.$C_d{}^{0.5}$ dominate the remaining frequencies in the 10 most directive events.

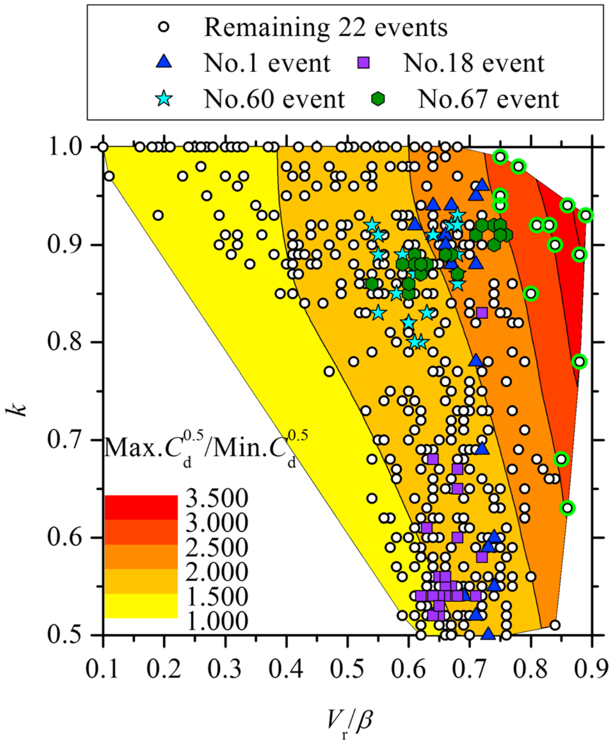

Figure 11. Distributions of variation of Max.C_d^{γ}/Min.C_d^{γ} values with the derived v_r/β and k values in the 26 events with weak or absent rupture directivity effects. Four events (Nos. 1, 18, 60, and 67) with potential rupture directivity discussed in detail in a later section were distinguished from the remaining 22 events represented by circles. Fourteen v_r/β-k plots from eight events (Nos. 16, 25, 44, 48, 53, 61, 69, and 71) at few frequencies falling into the zones characterized by Max.$C_d^{0.5}$/Min.$C_d^{0.5}$ > 2.5 were highlighted by green rings. Events corresponding to earthquake numbers are shown in Table S1 in the supporting information.

An event assumed as a simple line source model cannot rupture multiple frequency-dependent planes intersecting at the epicenter but toward different directions, as shown with the gray lines in Figure 12a. The strike of the rupture plane can be inferred from the retrieved φ value. Therefore, the reliability of the rupture parameters (i.e., v_r/β, φ, and k) can be evaluated by the stability of the strike of the rupture planes derived at different frequencies. In order to quantify the strike of the rupture plane, the deviation angle in the range from −90° to +90° was proposed, defined as the acute intersection angle between the rupture plane and an alignment passing through the epicenter. If the rupture plane coincided with the alignment after rotating anticlockwise within 90°, the deviation angle is positive; otherwise, it is negative. We first selected one from the two alignments (north–south trending and east–west trending alignments) for each event based on the preliminary trial calculation. The north–south trending alignment was first used to calculate the deviation angles for each event. The average of their absolute values at the 20 selected frequencies was then used to judge whether the north–south trending alignment was appropriate for each event. If the average value was not greater than 45°, the north–south trending alignment was valid; otherwise, another east–west trending alignment was adopted. Figure 12 a shows two examples illustrating how to determine the appropriate alignment: one selects north–south trending alignment for the No. 1 event, and the other selects east–west trending alignment for the No. 48 event. The deviation angles at the 20 frequencies for each event, calculated using the selected alignment, are plotted in Figure 12b. Substantial variability of the deviation angles over all considered frequencies, represented by the error bars, can be observed in 30 events (8 from the 10 most directive events in Table 1 and 22 from the remaining 26 events). However, the remaining six events (Nos. 49, 57, 1, 18, 60, and 67) show small variability of deviation angle (standard deviation <15°).

For each of the 10 most directive events in Table 1, the deviation angles were further divided into two groups according to the corresponding Max.$C_d^{0.5}$/Min.$C_d^{0.5}$ values: one group consisted of deviation angles at the directivity frequency band (in Table 1) with Max.$C_d^{0.5}$/Min.$C_d^{0.5}$ ≥ 2.5, and the other group covered those at the remaining frequencies. The standard deviations of the deviation angles in each group for the 10 most directive events and those covering all selected frequencies for the remaining 26 events were calculated and then plotted against the mean of the Max.$C_d^{0.5}$/Min.$C_d^{0.5}$ values over the corresponding frequencies, as shown in Figure 12c. The deviation

Table 1
Estimated Rupture Parameters, Including φ, v_r/β, and k for the 10 Most Directive Events

Event no.	Date (yyyy/mm/dd)	Time (hh:mm:ss)	Directivity frequency band (Hz)	f_c (Hz)[a]	φ[b]	v_r/β[b]	k[b]
5	2016/08/24	02:33:29	0.3–1.0	0.661	162.2 ± 3.3	0.85 ± 0.04	0.99 ± 0.01
9	2016/08/24	04:06:50	0.9–2.0	0.772	174.4 ± 1.9	0.82 ± 0.02	0.99 ± 0.01
20	2016/09/03	01:34:12	3.0–15.0	0.850	332.6 ± 4.8	0.82 ± 0.03	0.94 ± 0.01
32	2016/10/27	03:19:27	2.0–6.0	1.117	127.1 ± 10.8	0.80 ± 0.05	0.97 ± 0.01
34	2016/10/27	08:21:47	0.3–8.0	1.219	357.5 ± 18.5	0.82 ± 0.05	0.97 ± 0.02
42	2016/10/30	11:58:17	1.5–15.0	1.173	176.6 ± 3.4	0.89 ± 0.05	0.99 ± 0.01
49	2016/11/01	07:56:39	7.0–15.0	0.920	139.1 ± 1.9	0.81 ± 0.04	0.95 ± 0.03
56	2016/11/27	21:41:14	8.0–15.0	0.984	137.2 ± 6.7	0.76 ± 0.02	0.96 ± 0.01
57	2016/11/29	16:14:02	1.5–15.0	1.249	296.6 ± 2.0	0.88 ± 0.04	0.98 ± 0.01
58	2016/12/01	11:30:53	1.5–15.0	0.989	164.9 ± 4.8	0.85 ± 0.03	0.97 ± 0.01

[a] Computed from the nonparametric generalized inversion technique in this study. [b] Mean and the 1 standard deviation of the rupture parameters retrieved in the directivity frequency band (mean ± 1 standard deviation).

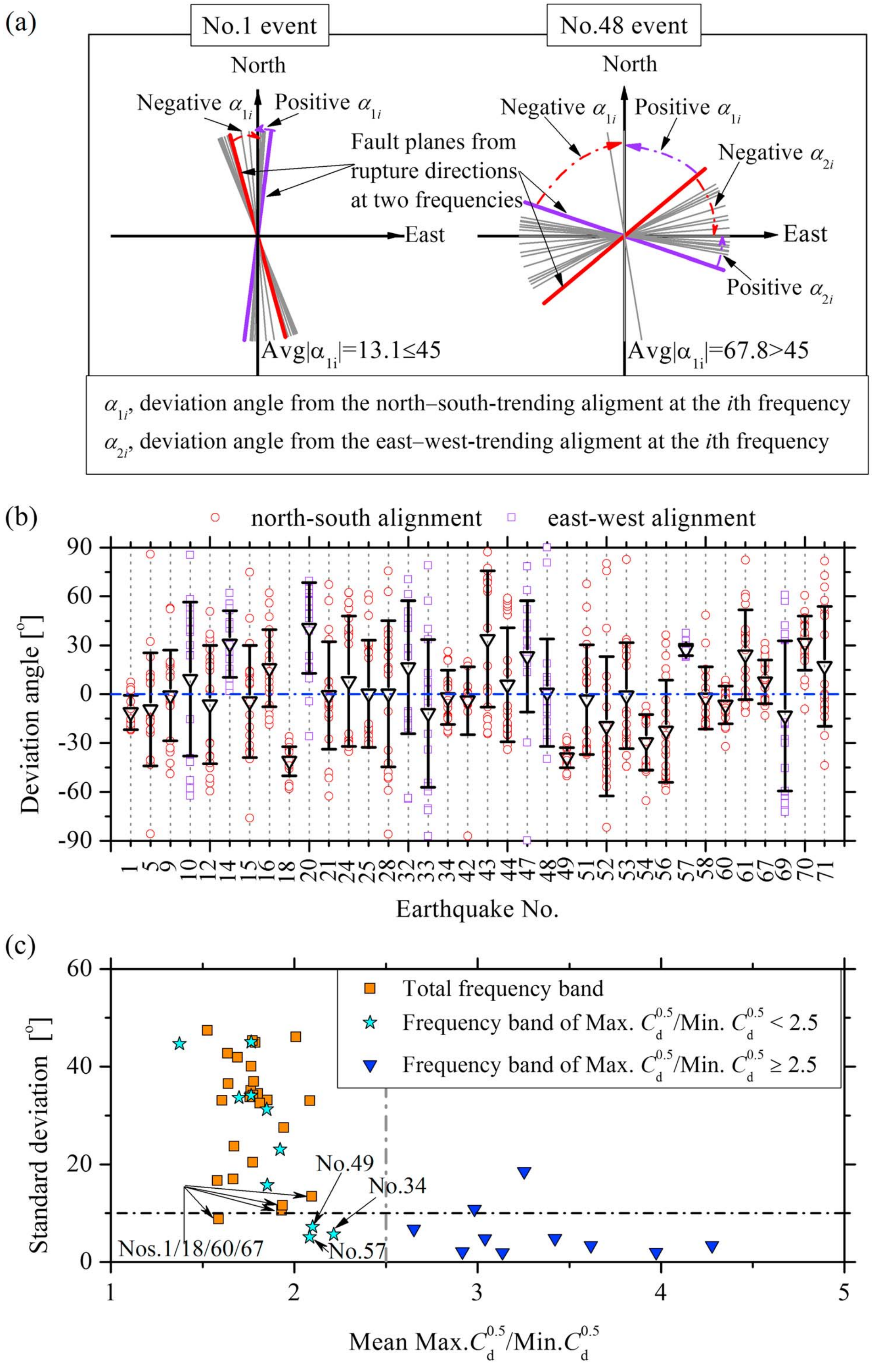

Figure 12. (a) Illustrations of how to determine appropriate alignment used to calculate the deviation angles. (b) Deviation angles of the rupture planes in the line source model hinted by the retrieved φ values from a north–south trending or east-west trending alignment at 20 frequencies considered for each event. Triangles (or squares) and error bars indicate the mean and 1 standard deviation of deviation angles over all frequencies. Events corresponding to earthquake numbers are shown in Table S1 in the supporting information. (c) Standard deviation of the deviation angles in each group for the 10 most directive events (i.e., Nos. 5, 9, 20, 32, 34, 42, 49, 56, 57, and 58) that reflect strong azimuthal variation and over the total frequencies for the remaining 26 events against the mean of the Max.$C_d^{0.5}$/Min.$C_d^{0.5}$ values. For the 10 most directive events, the deviation angles are classified into two groups (stars and triangles) according to the values of Max.$C_d^{0.5}$/Min.$C_d^{0.5}$.

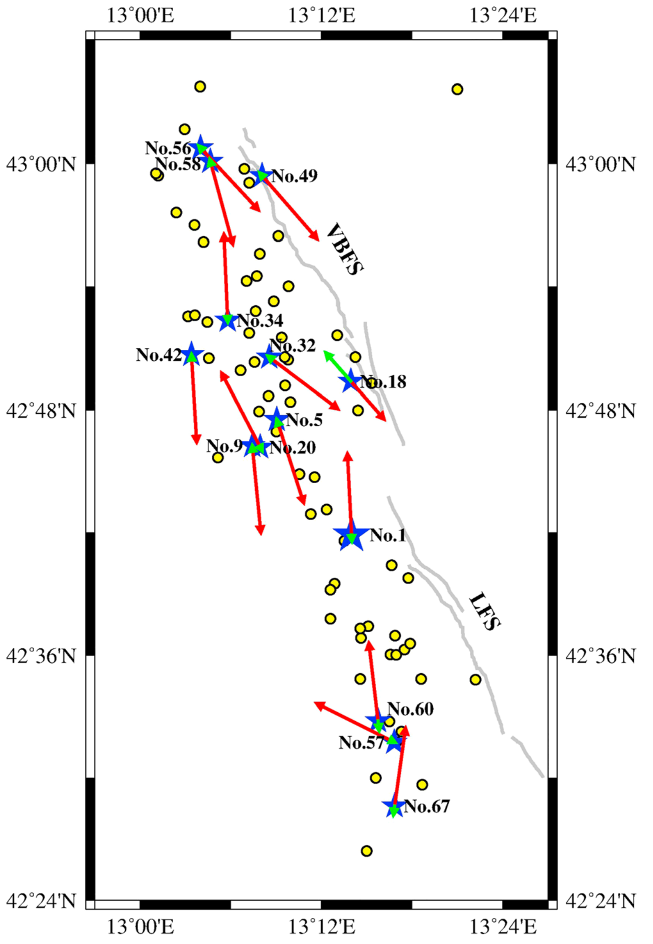

Figure 13. Directions of horizontal rupture propagation for the 14 events (represented by blue stars) discussed in this study. These events include the 10 most directive events listed in Table 1 (i.e., Nos. 5, 9, 20, 32, 34, 42, 49, 56, 57, and 58) and an additional four events (i.e., Nos. 1, 18, 60, and 67). Details of the events corresponding to earthquake numbers are shown in able S1 in the supporting information. Most events were identified as approximately unilateral and asymmetrical bilateral ruptures propagating predominantly in a certain direction, except for the No. 18 event as approximately bilateral rupture. The red and green arrow lines are applied to represent the predominant and secondary rupture directions, respectively. The length of the arrows represents the rupture proportion rather than the actual rupture length in the respective directions. Yellow dots indicate the epicenters of the other events used in this study. Gray lines represent the activated fault systems in this sequence. VBFS = Mt. Vettore-Mt. Bove fault system; LFS = Laga Mts. fault system.

angles in groups with Max.$C_d^{0.5}$/Min.$C_d^{0.5}$ ≥ 2.5 for the 10 most directive events generally produce small standard deviations (generally ≤10°), indicating the stability of the estimation of the rupture planes hinted by the φ values for the case of the significant azimuthal variation of apparent source spectra. The stable estimations preliminarily validate the reliability of the form of C_d^{γ} for describing the significant rupture directivity effects. Except for three events (Nos. 34, 49, and 57), for which relatively small variability was observed for both groups (Figure 12c), large variability of the deviation angles was found for the group with small Max.$C_d^{0.5}$/Min. $C_d^{0.5}$ values (<2.5) in the other seven events, indicating unstable estimation of the rupture planes hinted by the φ values for cases of weak or absent rupture directivity effects. Similarly, large variability of the deviation angles covering all selected frequencies was generally observed in most of the remaining 26 events, for which weak or absent rupture directivity was supposed. We thus inferred that the form of C_d^{γ} is unqualified to express weak or absent rupture directivity effects. However, small variability of the deviation angles was observed in four of the 26 events (Nos. 1, 18, 60, and 67), which might suggest the occurrence of potential rupture directivity. The rupture properties for the four events were also discussed in detail in the later section.

The means and standard deviations for the retrieved rupture parameters (v_r/β, φ, and k) within the directivity frequency bands of Max.$C_d^{0.5}$/Min. $C_d^{0.5}$ ≥ 2.5 for the 10 most directive events are provided in Table 1. The φ values confirmed that the ruptures are indeed on the NNW–SSE striking fault plane, which is close to the NNW–SSE trending seismogenic fault systems and the major axis of the spatial distribution of the nucleated region of the 2016–2017 seismic sequence (Figure 1). The k values (mainly >0.95) consistently reveal approximately unilateral rupture propagation for the 10 most directive events. Some events (Nos. 20, 34, and 57) propagated toward the northwest, whereas other events (Nos. 5, 9, 32, 42, 49, 56, and 58) propagated toward the southeast. The rupture directivity for three events (Nos. 5, 49, and 57) discussed in our study were also investigated by Calderoni et al. (2017). They also identified unilateral rupture propagation toward the southeast for the Nos. 5 and 49 events and toward the northwest for the No. 57 event. The retrieved v_r/β values are mainly within the range 0.80–0.90, indicating fast rupture velocity for the 10 events. Given $c = 3.15$ km/s at the depth of 7.5–14.5 km, following the central Italy Apennines velocity model (Herrmann et al., 2011), the rupture velocity is approximately in the range 2.52–2.84 km/s. The approximately unilateral rupture propagation and the reasonably fast rupture velocity reveal strong rupture directivity effects in the 10 most directive events.

For the No. 1 event, the symmetrical bilateral rupture propagation ($k = 0.54 \pm 0.04$) on the NNW–SSE trending fault plane ($\varphi = 340.7 \pm 2.6$) with v_r/β of ~0.71 at low frequencies (0.3–1.0 Hz) and the asymmetrical bilateral rupture with ~90% of the rupture propagating ($k = 0.92 \pm 0.03$) in the north direction ($\varphi = 357.1 \pm 8.7$) with v_r/β of ~0.67 at high frequencies (3.0–15.0 Hz) were obtained according to the retrieved rupture parameters in our study. Different results for this event have been determined by some previous studies using data with different frequency bands. The kinematic rupture histories separately inverted by Tinti et al. (2016) and by Pizzi et al. (2017) using low-frequency waveforms of strong-motion recordings, or jointly inverted by Liu et al. (2017) by incorporating data sets of low-frequency strong-motion waveforms, teleseismic waveforms, and GPS data, exhibited the bilateral rupture propagation in the NNW and SSE directions. However, asymmetrical bilateral rupture propagation with clear NNW trending predominance (~70%) was confirmed by Calderoni et al. (2017) who investigated high-frequency S wave amplitude variations versus azimuths. Similarly, predominantly unilateral rupture with prevailing northward direction of rupture propagation was also reported by Ren, Wang, and Wen (2017) using observed PGAs and peak ground velocities. It implies that the results of identification of rupture directivity are reliant on the frequency-dependent measurement data used. The rupture velocity of the No. 1 event, that is, ~2.45 km/s (given $c = 3.15$ km/s at the depth of 8 km; Herrmann et al., 2011), was found close to the value of 2.52 km/s (given $c = 3.15$ km/s) provided by Convertito et al. (2017) but much slower than the value of ~3.0 km/s reported by Pizzi et al. (2017) and by Tinti et al. (2016). The rupture of the No. 18 event was identified as bilateral rupture propagation ($k = 0.57 \pm 0.08$), and slight predominance of rupture propagation in the ~SE direction (N138.8°) was found. However, the Nos. 60 and 67 events were evidently asymmetrical bilateral ruptures with ~90% of the rupture propagation ($k = 0.88 \pm 0.04$, and 0.89 ± 0.02, respectively) in the NNW direction (~N350.0°) for the No. 60 event and in the NNE direction (~N8.0°) for the No. 67 event. Calderoni et al. (2017) also identified both events (Nos. 60 and 67) as unilateral ruptures in the NNW direction. The slow rupture velocities for the three events (Nos. 18, 60, and 67) were confirmed by v_r/β of ~0.65.

The directions of horizontal rupture propagation for the 10 most directive events in Table 1 and the additional four events (Nos. 1, 18, 60, and 67) are shown in Figure 13. Results at high frequency for the No.1 event only are shown. The lengths of the arrows represent the rupture proportions and not the actual rupture lengths in the respective directions. SSE or SEE rupture directivity is a common feature for most events located in the northern area of the No. 1 event; however, the opposite rupture directivity (NNW or NNE) dominates those events located in the southern area. Similar prevailing rupture directivity was also confirmed by Calderoni et al. (2017) for this sequence.

7. Conclusions

In this study, we applied the two-step nonparametric GIT to separate simultaneously the source spectra, path attenuation terms, and site responses from the S wave Fourier amplitude spectra of 5,135 selected strong-motion data recorded in 78 events of $M_L = 3.5–6.1$ during the 2016–2017 central Italy seismic sequence. We analyzed the propagation path attenuation and the source characteristics for this sequence. From the inverted path attenuation terms, we revealed the geometrical spreading was R^{-1} and the frequency-dependent quality factors were regressed as $96.56f^{0.58}$ in the seismogenic area, which are highly consistent with those in the 1997 Umbria-Marche seismogenic area. However, path attenuation in this study region was found generally weaker than in the 2009 L'Aquila seismogenic area.

Inverted source spectra were used to calculate the source parameters, including the seismic moment (M_0), corner frequency (f_c), and stress drop ($\Delta\sigma$), according to the ω-square source model. The calculated $\Delta\sigma$ values for this seismic sequence were found mainly in the range 0.113 to 12.190 MPa. The $\Delta\sigma$ values for events of $M_w = 3.58–4.73$ were found in the range 0.113 to 2.905 MPa with a mean of 0.709 MPa and standard deviation of 0.333 on the base-10 logarithmic scale, and they showed a slight trend of increase with increasing M_w. However, the $\Delta\sigma$ values for events of $M_w = 4.89–6.13$ were in the range 5.475 to 12.190 MPa with a mean of 7.149 MPa. The increasing stress drops with the event size can be explained by the considerably less increase of slip with rupture dimension in a strongly heterogeneous stress field than in a relatively homogeneous stress field, which was hinted by the high variability in $\Delta\sigma$ values for smaller events. The $\Delta\sigma$ values revealed obvious dependence on M_w over the range 3.58–6.13, indicating the breakdown of earthquake self-similar scaling in this seismic sequence. The significant depth independence and scattered spatial distribution within the epicentral area for high-$\Delta\sigma$ events further verified the dependence between $\Delta\sigma$ and M_w.

We selected 36 events to investigate source rupture directivity according to the azimuthal dependence in the apparent source spectra. The residuals between the apparent source spectra and the inverted mean source spectrum on the base-10 logarithmic scale were calculated to reveal the azimuthal dependence. The form of ${C_d}^{\gamma}$ expressed by the source rupture parameters under the assumption of line source model, including φ, v_r/β, and k, was applied to fit the azimuthal residuals. Residuals at 20 frequencies selected from 0.3 to 15.0 Hz for each event were considered for the estimations of rupture parameters. The fitting showed that the $\log_{10}({C_d}^{\gamma})$ curves generally matched well the azimuthal residuals irrespective of the value of γ selected. Different γ values were first used to test the retrieved source rupture parameters. Results indicated that the use of $\gamma = 0.5$ in ${C_d}^{\gamma}$ was optimal for explaining the azimuthal residuals, in that the retrieved γ values were mostly in the range 0.6–0.9, which is commonly used by the seismology community.

The large values at directivity frequency bands with Max.$C_d^{0.5}$/Min.$C_d^{0.5} \geq 2.5$ in only 10 events revealed the strong azimuthal variation of the apparent source spectra. The remaining 26 events show very small Max.$C_d^{0.5}$/Min.$C_d^{0.5}$ values at most frequencies considered, indicating the weak or absent rupture directivity effects. The form of C_d^{γ} is qualified to describe the strong rupture directivity effects, rather than the weak or absent directivity effects, inferred from the stability of the rupture planes hinted by the φ estimations. The rupture parameters obtained for the 10 most directive events at the directivity frequency bands all confirmed the approximately unilateral rupture propagation on the NNW–SSE striking fault plane with a reasonably fast rupture velocity, that is, ~2.52–2.84 km/s. The fact that the directivity frequency bands were generally found over the source corner frequency revealed the frequency dependence of rupture directivity.

Stable φ estimations were also observed in the additional four events (Nos. 1, 18, 60, and 67), although small Max.$C_d^{0.5}$/Min.$C_d^{0.5}$ values were found for most of the selected frequencies. The No. 1 event showed symmetrical bilateral rupture at low frequencies (0.3–1.0 Hz) and asymmetrical bilateral rupture with ~90% in the north direction at high frequencies (1.0–15.0 Hz). The No. 18 event had approximately symmetrical bilateral rupture propagation on the approximately NW–SE striking fault plane, whereas the Nos. 60 and 67 events were identified as asymmetrical bilateral rupture propagations with ~90% rupture propagation in the NNW and NNE directions, respectively. The four events all showed reasonably slow rupture velocities (~2.05 km/s).

According to the rupture parameters of the 14 events (10 most directive events and an additional 4 events), we note that SSE or SEE rupture directivity was a common feature for events located to the north of the 24 August mainshock (No. 1), whereas the opposite rupture directivity (NNW or NNE) dominated events to the south.

Acknowledgments

Basic information for earthquakes, including epicentral location, hypocentral depth, and local magnitude, was obtained from INGV Centro Nazionale Terremoti (http://cnt.rm.ingv.it/, last accessed October 2017). The time domain moment tensor (TDMT) solutions of INGV were available at the website of http://cnt.rm.ingv.it/en/tdmt (last accessed October 2017). The strong-motion data were derived from the Engineering Strong-Motion (ESM) database accessible at the website of http://esm.mi.ingv.it/ (last accessed October 2017). We are very grateful to the anonymous reviewers for their valuable comments that improved this article. This work was supported by the National Key R&D Program of China (No. 2017YFC1500801), National Natural Science Foundation of China (Nos. 51778589 and 51808514), Natural Science Foundation of Heilongjiang Province (No. E2017065), and Science Foundation of the Institute of Engineering Mechanics, CEA (No. 2016A04).

References

Abrahamson, N. A., & Silva, W. J. (1997). Empirical response spectral attenuation relations for shallow crustal earthquakes. *Seismological Research Letters*, *68*(1), 94–127. https://doi.org/10.1785/gssrl.68.1.94

Aki, K. (1967). Scaling law of seismic spectrum. *Journal of Geophysical Research*, *72*(4), 1217–1231. https://doi.org/10.1029/JZ072i004p01217

Allmann, B. P., & Shearer, P. M. (2009). Global variations of stress drop for moderate to large earthquakes. *Journal of Geophysical Research*, *114*, B01310. https://doi.org/10.1029/2008JB005821

Amato, A., Azzara, R., Chiarabba, C., Cimini, G. B., Cocco, M., Bona, M. D., et al. (1998). The 1997 Umbria–Marche, Italy, earthquake sequence: A first look at the main shocks and aftershocks. *Geophysical Research Letters*, *25*(15), 2861–2864. https://doi.org/10.1029/98GL51842

Ameri, G., Oth, A., Pilz, M., Bindi, D., Parolai, S., Luzi, L., et al. (2011). Seperation of source and site effects by generalized inversion technique using the aftershock recordings of the 2009 L'Aquila earthquake. *Bulletin of Earthquake Engineering*, *9*(3), 717–739. https://doi.org/10.1007/s10518-011-9248-4

Anderson, J. G., & Hough, S. E. (1984). A model for the shape of the Fourier amplitude spectrum of acceleration at high frequencies. *Bulletin of the Seismological Society of America*, *74*(5), 1969–1993.

Atkinson, G. M. (2004). Empirical attenuation of ground-motion spectral amplitudes in southeastern Canada and the northeastern United States. *Bulletin of the Seismological Society of America*, *94*(3), 1079–1095. https://doi.org/10.1785/0120030175

Atkinson, G. M., & Cassidy, J. F. (2000). Integrated use of seismography and strong-motion data to determine soil amplification: Response of the Fraser River Delta to the Duvall and Georgia Strait earthquakes. *Bulletin of the Seismological Society of America*, *90*(4), 1028–1040. https://doi.org/10.1785/0119990098

Ben-Menahem, A. (1961). Radiation of seismic surface-waves from finite moving sources. *Bulletin of the Seismological Society of America*, *51*(3), 401–435.

Ben-Zion, Y. (2008). Collective behavior of earthquakes and faults: Continuum-discrete transitions, progressive evolutionary changes, and different dynamic regimes. *Reviews of Geophysics*, *46*, RG4006. https://doi.org/8755-1209/08/2008RG000260

Ben-Zion, Y., Eneva, M., & Liu, Y. (2003). Large earthquake cycles and intermittent criticality on heterogeneous faults due to evolving stress and seismicity. *Journal of Geophysical Research*, *108*(B6), 2307. https://doi.org/10.1029/2002JB002121

Ben-Zion, Y., & Zhu, L. (2002). Potency-magnitude scaling relations for southern California earthquakes with $1.0 < M_L < 7.0$. *Geophysical Journal International*, *148*(3), F1–F5. https://doi.org/10.1046/j.1365-246X.2002.01637.x

Beresnev, I. A., Wen, K.-L., & Yeh, Y. T. (1995). Nonlinear soil amplification: Its corroboration in Taiwan. *Bulletin of the Seismological Society of America*, *85*(2), 456–515.

Bernard, P., Herrero, A., & Berge, C. (1996). Modeling directivity of heterogeneous earthquake ruptures. *Bulletin of the Seismological Society of America*, *86*(4), 1149–1160.

Bindi, D., Castro, R. R., Franceschina, G., Luzi, L., & Pacor, F. (2004). The 1997–1998 Umbria–Marche sequence (central Italy): Source, path, and site effects estimated from strong motion data recorded in the epicentral area. *Journal of Geophysical Research*, *109*, B04312. https://doi.org/10.1029/2003JB002857

Bindi, D., Pacor, F., Luzi, L., Massa, M., & Ameri, G. (2009). The M_w 6.3, 2009 L'Aquila earthquake: Source, path, and site effects from spectral analysis of strong motion data. *Geophysical Journal International*, *179*(3), 1573–1579. https://doi.org/10.1111/j.1365-246X.2009.04392.x

Bindi, D., Spallarossa, D., Augliera, P., & Cattaneo, M. (2001). Source parameters estimated from the aftershocks of the 1997 Umbria–Marche (Italy) seismic sequence. *Bulletin of the Seismological Society of America*, *91*(3), 448–455. https://doi.org/10.1785/0120000084

Bindi, D., Spallarossa, D., & Pacor, F. (2017). Between-event and between-station variability observed in the Fourier and response spectra domains: Comparison with seismological models. *Geophysical Journal International*, *210*, 1092–1104. https://doi.org/10.1093/gji/ggx217

Boatwright, J. (2007). The persistence of directivity in small earthquakes. *Bulletin of the Seismological Society of America*, *97*(6), 1850–1861. https://doi.org/10.1785/0120050228

Boore, D. M., & Boatwright, J. (1984). Average body-wave radiation coefficients. *Bulletin of the Seismological Society of America*, *74*(5), 1615–1621.

Brune, J. N. (1970). Tectonic stress and the spectra of seismic shear waves from earthquakes. *Journal of Geophysical Research*, *75*(26), 4997–5009. https://doi.org/10.1029/JB075i026p04997

Calderoni, G., Rovelli, A., Ben-Zion, Y., & Giovambattista, R. D. (2015). Along-strike rupture directivity of earthquakes of the 2009 L'Aquila, central Italy, seismic sequence. *Geophysical Journal International*, *203*, 399–415. https://doi.org/10.1093/gji/ggv275

Calderoni, G., Rovelli, A., & Giovambattista, R. D. (2017). Rupture directivity of the strongest 2016–2017 central Italy earthquakes. *Journal of Geophysical Research: Solid Earth*, *122*, 9118–9131. https://doi.org/10.1002/2017JB014118

Campbell, K. W. (2009). Estimates of shear-wave Q and κ_0 for unconsolidated and semiconsolidated sediments in eastern North America. *Bulletin of the Seismological Society of America*, *99*(4), 2365–2392. https://doi.org/10.1785/0120080116

Castro, R. R., Anderson, J. G., & Singh, S. K. (1990). Site response, attenuation and source spectra of S waves along the Guerrero, Mexico, subduction zone. *Bulletin of the Seismological Society of America*, *80*(6), 1481–1503.

Cheloni, D., de Novellis, V., Albano, M., Antonioli, A., Anzidei, M., Atzori, S., et al. (2017). Geodetic model of the 2016 central Italy earthquake sequence inferred from InSAR and GPS data. *Geophysical Research Letters*, *44*, 6778–6787. https://doi.org/10.1002/2017GL073580

Chen, K. H., Bürgmann, R., & Nadeau, R. M. (2013). Do earthquakes talk to each other? Triggering and interaction of repeating sequences at Parkfield. *Journal of Geophysical Research: Solid Earth*, *118*, 165–182. https://doi.org/10.1029/2012JB009486

Chiarabba, C., Amato, A., Anselmi, M., Baccheschi, P., Bianchi, I., Cattaneo, M., et al. (2009). The 2009 L'Aquila (central Italy) M_{w}6.3 earthquake: Main shock and aftershocks. *Geophysical Research Letters*, *36*, L18308. https://doi.org/10.1029/2009GL039627

Chiaraluce, L., di Stefano, R., Tinti, E., Scognamiglio, L., Michele, M., Casarotti, E., et al. (2017). The 2016 central Italy seismic sequence: A first look at the mainshocks, aftershocks, and source models. *Seismological Research Letters*, *88*(3), 757–771. https://doi.org/10.1785/0220160221

Convertito, V., de Matteis, R., & Pino, N. A. (2017). Evidence for static and dynamic triggering of seismicity following the 24 August 2016, $M_{\mathrm{W}} = 6.0$, Amatrice (central Italy) earthquake. *Pure and Applied Geophysics*, *174*(10), 3663–3672. https://doi.org/10.1007/s00024-017-1559-1

Cultrera, G., Pacor, F., Franseschina, G., Emolo, A., & Cocco, M. (2009). Directivity effects for moderate-magnitude earthquakes (Mw 5.6–6.0) during the 1997 Umbria–Marche sequence, central Italy. *Tectonophysics*, *476*(1-2), 110–120. https://doi.org/10.1016/j.tecto.2008.09.022

Drouet, S., Bouin, M.-P., & Cotton, F. (2011). New moment magnitude scale, evidence of stress drop magnitude scaling and stochastic ground motion model for the French West Indies. *Geophysical Journal International*, *187*(3), 1625–1644. https://doi.org/10.1111/j.1365-246X.2011.05219.x

Fisher, D. S., Dahmen, K., Ramanathan, S., & Ben-Zion, Y. (1997). Statistics of earthquakes in simple models of heterogeneous faults. *Physical Review Letters*, *78*(25), 4885–4888. https://doi.org/10.1103/PhysRevLett.78.4885

Gallovič, F. (2016). Modeling velocity recordings of the Mw 6.0 south Napa, California, earthquake: Unilateral event with weak high-frequency directivity. *Seismological Research Letters*, *87*(1), 2–14. https://doi.org/10.1785/0220150042

Hanks, T. C., & Kanamori, H. (1979). A moment magnitude scale. *Journal of Geophysical Research*, *84*(B5), 2348–2350. https://doi.org/10.1029/JB084iB05p02348

Herrmann, R. B., Malagnini, L., & Munafò, I. (2011). Regional moment tensors of the 2009 L'Aquila earthquake sequence. *Bulletin of the Seismological Society of America*, *101*(3), 975–993. https://doi.org/10.1785/0120100184

Husid, P. (1967). *Gravity effects on the earthquake response of yielding structures*. Pasadena, CA: California Institute of Technology.

Joyner, W. B. (1991). Directivity for non-uniform ruptures. *Bulletin of the Seismological Society of America*, *81*(4), 1391–1395.

Kanamori, H., & Rivera, L. (2004). Static and dynamic scaling relations for earthquakes and their implications for rupture speed and stress drop. *Bulletin of the Seismological Society of America*, *94*(1), 314–319. https://doi.org/10.1785/0120030159

Kane, D. L., Shear, P. M., Goertz-Allmann, B. P., & Vernon, F. L. (2013). Rupture directivity of small earthquakes at Parkfield. *Journal of Geophysical Research: Solid Earth*, *118*, 212–221. https://doi.org/10.1029/2012JB009675

Kenner, S. J., & Simons, M. (2005). Temporal clustering of major earthquakes along individual faults due to post-seismic reloading. *Geophysical Journal International*, *160*, 179–194. https://doi.org/10.1111/j.1365-246X.2005.02460.x

Kilb, D., Biasi, G., Anderson, J., Brune, J., Peng, Z., & Vernon, F. L. (2012). A comparison of spectral parameter kappa from small and moderate earthquakes using southern California ANZA seismic network data. *Bulletin of the Seismological Society of America*, *102*(1), 284–300. https://doi.org/10.1785/0120100309

Konno, K., & Ohmachi, T. (1998). Ground-motion characteristics estimated from ratio between horizontal and vertical components of microtremor. *Bulletin of the Seismological Society of America*, *88*(1), 228–241.

Ktenidou, O.-J., Gélis, C., & Bonilla, L.-F. (2013). A study on the variability of kappa (κ) in a borehole: Implications of the computation process. *Bulletin of the Seismological Society of America*, *103*(2A), 1048–1068. https://doi.org/10.1785/0120120093

Liu, C., Zheng, Y., Xie, Z., & Xiong, X. (2017). Rupture features of the 2016 M_{w} 6.2 Norcia earthquake and its possible relationship with strong seismic hazards. *Geophysical Research Letters*, *44*, 1320–1328. https://doi.org/10.1002/2016GL071958

Luzi, L., Pacor, F., Puglia, R., Lanzano, G., Felicetta, C., D'Amico, M., et al. (2017). The Central Italy seismic sequence between August and December 2016: Analysis of strong-motion observations. *Seismological Research Letters*, *88*(5), 1219–1231. https://doi.org/10.1785/0220170037

McGuire, J. J., Zhao, L., & Jordan, T. H. (2002). Predominance of unilateral rupture for a global catalog of large earthquakes. *Bulletin of the Seismological Society of America*, *92*(8), 3309–3317. https://doi.org/10.1785/0120010293

McNamara, D., Meremonte, M., Maharrey, J. Z., Mildore, S.-L., Altidore, J. R., Anglade, D., et al. (2012). Frequency-dependent seismic attenuation within the Hispaniola Island region of the Caribbean Sea. *Bulletin of the Seismological Society of America*, *102*(2), 773–782. https://doi.org/10.1785/0120110137

Oth, A. (2013). On the characteristics of earthquake stress release variations in Japan. *Earth and Planetary Science Letters*, *377–378*, 132–141. http://doi.org/10.1016/j.epsl.2013.06.037

Oth, A., Bindi, D., Parolai, S., & Giacomo, D. D. (2011). Spectral analysis of K-NET and KiK-net data in Japan, part II: On attenuation characteristics, source spectra, and site response of borehole and surface stations. *Bulletin of the Seismological Society of America*, *102*(2), 667–687. https://doi.org/10.1785/0120100135

Oth, A., Bindi, D., Parolao, S., & Giacomo, D. D. (2010). Earthquake scaling characteristics and the scale-(in)dependence of seismic energy-to-moment ratio: Insights from KiK-net data in Japan. *Geophysical Research Letters*, *37*, L19304. https://doi.org/10.1029/2010GL044572

Oth, A., & Kaiser, A. E. (2014). Stress release and source scaling of the 2010–2011 Canterbury, New Zealand, earthquake sequence from spectral inversion of ground motion data. *Pure and Applied Geophysics*, *171*(10), 2767–2782. https://doi.org/10.1007/s00024-013-0751-1

Pacor, F., Gallovič, F., Puglia, R., Luzi, L., & D'Amico, M. (2016). Diminishing high-frequency directivity due to a source effect: Empirical evidence from small earthquakes in the Abruzzo region, Italy. *Geophysical Research Letters*, *43*, 5000–5008. https://doi.org/10.1002/2016GL068546

Pacor, F., Spallarossa, D., Oth, A., Luzi, L., Puglia, R., Cantore, L., et al. (2016). Spectral models for ground motion prediction in the L'Aquila region (central Italy): Evidence for stress-drop dependence on magnitude and depth. *Geophysical Journal International*, *204*(2), 697–718. https://doi.org/10.1093/gji/ggv448, https://doi.org/10.1093/gji/ggv448

Pavel, F., & Vacareanu, R. (2018). Investigation of regional attenuation of Vrancea (Romania) intermediate-depth earthquakes. *Earthquake Engineering and Engineering Vibration*, *17*(3), 501–509. https://doi.org/10.1007/s11803-018-0458-5

Pizzi, A., Domenica, A. D., Gallovič, F., Luzi, L., & Puglia, R. (2017). Fault segmentation as constraint to the occurrence of the main shocks of the 2016 central Italy seismic sequence. *Tectonics*, *36*, 2370–2387. https://doi.org/10.1002/2017TC004652

Régnier, J., Cadet, H., Bonilla, L. F., Bertrand, E., & Semblat, J.-F. (2013). Assessing nonlinear behavior of soils in seismic site response: Statistical analysis on KiK-net strong-motion data. *Bulletin of the Seismological Society of America*, *103*(3), 1750–1770. https://doi.org/10.1785/0120120240

Ren, Y., Wang, H., & Wen, R. (2017). Imprint of rupture directivity from ground motions of the 24 August 2016 M_w6.2 central Italy earthquake. *Tectonics*, *36*, 3178–3191. https://doi.org/10.1002/2017TC004673

Ren, Y., Wen, R., Yao, X., & Ji, K. (2017). Five parameters for the evaluation of the soil nonlinearity during the Ms8.0 Wenchuan earthquake using the HVSR method. *Earth Planets & Space*, *69*(1), 116. https://doi.org/10.1186/s40623-017-0702-7

Rovida, A., Locati, M., Camassi, R., Lolli, B., & Gasperini, P. (2016). CPT2015, the 2015 version of the parametric catalogue of Italian earthquakes. Rome: Istituto Nazionale di Geofisica e Vulcanologia. https://doi.org/10.6092/INGV.IT-CPTI15.

Ruiz, J. A., Baumont, D., Bernard, P., & Berge-Thierry, C. (2011). Modeling directivity of strong ground motion with a fractal, k^{-2}, kinematic source model. *Geophysical Journal International*, *186*(1), 226–244. https://doi.org/10.1111/j.1365-246X.2011.05000.x

Scognamiglio, L., Tinti, E., Casarotti, E., Pucci, S., Villani, F., Cocco, M., et al. (2018). Complex fault geometry and rupture dynamics of the $\mathrm{M_w}$ 6.5, 2016, October 30th central Italy earthquake. *Journal of Geophysical Research: Solid Earth*, *123*, 2943–2964. https://doi.org/10.1002/2018JB015603

Siddiqqi, J., & Atkinson, G. M. (2002). Ground-motion amplification at rock sites across Canada as determined from the horizontal-to-vertical components ratio. *Bulletin of the Seismological Society of America*, *92*(2), 877–884. https://doi.org/10.1785/0120010155

Stucchi, M., Meletti, C., Montaldo, V., Crowley, H., Calvi, G. M., & Boschi, E. (2011). Seismic hazard assessment (2003–2009) for the Italian building code. *Bulletin of the Seismological Society of America*, *101*(4), 1885–1911. https://doi.org/10.1785/0120100130

Tan, Y., & Helmberger, D. (2010). Rupture directivity characteristics of the 2003 Big Bear sequence. *Bulletin of the Seismological Society of America*, *100*(3), 1089–1106. https://doi.org/10.1785/0120090074

Tinti, E., Scognamiglio, L., Michelini, A., & Cocco, M. (2016). Slip heterogeneity and directivity of the M_L 6.0, 2016, Amatrice earthquake estimated with rapid finite-fault inversion. *Geophysical Research Letters*, *43*, 10,745–10,752. https://doi.org/10.1002/2016GL071263

Wang, H., Ren, Y., & Wen, R. (2018). Source parameters, path attenuation and site effects from strong-motion recordings of the Wenchuan aftershocks (2008–2013) using a non-parametric generalized inversion technique. *Geophysical Journal International*, *212*(2), 872–890. https://doi.org/10.1093/gji/ggx447

Wen, R., Wang, H., & Ren, Y. (2015). Rupture directivity from strong-motion recordings of the 2013 Lushan aftershocks. *Bulletin of the Seismological Society of America*, *105*(6), 3068–3082. https://doi.org/10.1785/0120150100